Preparation and electroanalytical applications of vertically aligned carbon nanotubes

Tiago Almeida Silva,[a] Hudson Zanin,[b] Evaldo José Corat,[c] Paul W. May[d] and Orlando Fatibello-Filho*[a]

1 Introduction

Since the first carbon nanotubes (CNTs) were produced by Iijima in 1991[1] and 1993,[2] these carbon nanomaterials have aroused great interest in various technological sectors, being one of the most widely investigated and applied materials of the nanotechnology field.[3,4] At a structural level, a CNT can be understood as a graphene sheet (composed of carbon atoms with sp^2 hybridisation) rolled up in a cylindrical/tubular shape.[4,5] The ends or tips of the CNTs are either open, or closed in a fullerene-type hemispherical shape. CNTs are classified into two different classes: (1) Single-Walled Carbon Nanotubes ("SWCNT") and (2) Multi-Walled Carbon Nanotubes ("MWCNT"). The basic structural difference between these two CNTs forms is the number of concentric nanotubes. As its name suggests, SWCNT have only one graphene sheet layer rolled in the tube form, while MWCNT consist of two or more concentric nanotubes,[3–5] as shown in Fig. 1.

The time, money and scientific effort invested in the development of CNT-based technologies are due to their unique optical, electronic and mechanical properties.[3–5] Currently, CNTs are easy and cheap to manufacture, enabling large areas and well adherent coatings. The numerous applications of CNTs include areas of development of electronic devices, energy storage devices, catalysis, as an adsorbent in wastewater treatment, sensors for gases and biological sensors (biosensors), and when combined with other materials such as polymers and fibers, CNTs serve as reinforcing agents forming composites with excellent mechanical properties.[3,6–10] In addition to these applications, CNTs can be used as electrodes in a variety of electrochemical devices, especially electrochemical (bio)sensors. CNTs possess a set of intrinsic characteristics that

[a]Department of Chemistry, Federal University of São Carlos, Rod. Washington Luís km 235, São Carlos, P. O. Box 676, CEP: 13560-970, SP, Brazil. E-mail: bello@ufscar.br

[b]Laboratory of Energy Storage & Supply (ES&S), Institute of Research and Development (IP&D), Univap, Av. Shishima Hifumi 2911, São José dos Campos, CEP: 12224-000, SP, Brazil

[c]National Institute for Space Research, Av. dos Astronautas 1758, São José dos Campos, CEP: 12227-010, SP, Brazil

[d]School of Chemistry, University of Bristol, Cantocks Close, Bristol BS8 1TS, United Kingdom
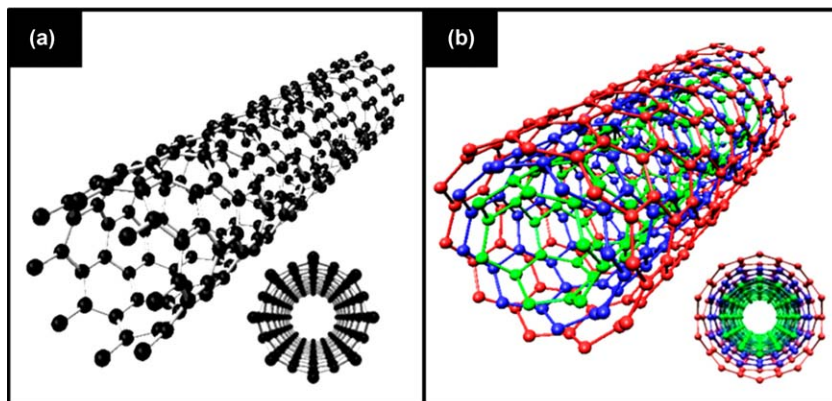
Fig. 1 Schematic representation of a (a) SWCNT and (b) MWCNT.

make them ideal candidates for use in electrochemistry. In general, they are excellent electrical conductors, providing high electron-transfer rates, have a high surface area, and when functionalised, can be easily used as a matrix for the immobilisation of numerous chemical and biological species, such as metal complexes, enzymes, proteins, *etc.* The improved electron-transfer rates enables the detection of analytes at lower working potentials than those presented by electrodes made from other materials, and, moreover, the use of CNTs leads to an increase of the analytical signal, which can generate more sensitive electroanalytical procedures and with ever lower detection levels.[4,11]

A number of studies were conducted to elucidate the mechanisms of electron transfer in CNTs, and to determine the physical and chemical features which influence the CNT electrochemistry. In the next sections, we will assess the electrochemistry of CNTs, and demonstrate that the orientation of the CNTs is an important factor affecting the electrochemical performance of these electrodes. Thus, special attention will be paid to the recent trends in the preparation, functionalisation and characterisation of oriented carbon nanotubes, and an extensive review of recent advances in the use of vertically aligned carbon nanotubes (VACNT) electrodes for the establishment of new electroanalytical methods also will be presented.

2 Electrochemistry of carbon nanotubes

Electrochemical applications of CNTs as electrodes have greatly increased in recent years mainly due to their outstanding properties, such as fast electron-transfer kinetics (high heterogeneous electron-transfer constant, k^0),[12] high electroactive surface area, chemical stability and easy handling. CNT electrodes can be prepared in several ways, for instance, by drop-casting,[13] spraying dispersion[14] and electrophoretic deposition in resin or mineral oil composites.[15–17] The general consensus is that the incorporation of CNTs improves the analytical response of an electrode.[18–26]

A series of comparative cyclic voltammetric studies of CNT electrodes with electrodes made from the basal plane of highly oriented pyrolytic graphite (HOPG) were performed using the redox couple potassium ferricyanide and ferrocyanide ($K_3[Fe(CN)_6]/K_4[Fe(CN)_6]$, respectively) by Banks et al.[18] and Moore et al.[19] They reported that the separation between the oxidation and reduction peaks (ΔE_p) depends on the type of carbon electrode and the nature of the particular surface used in the measurement. For modified CNT electrodes, ΔE_p was about 58 mV, whereas values were obtained of 78 mV from the edge plane and 350 mV from the basal plane of HOPG electrodes. Streeter et al.[20] observed that the ΔE_p in a one-electron oxidation or reduction could be even smaller ~ 58 mV (as expected from Nernst equation) when one employs CNTs electrodes. They explained it by a 'thin layer effect', which describes the restriction of diffusion of electroactive species trapped in the pores of a CNT electrode. Furthermore, this same group conducted studies to evaluate the effect of metal impurities on the electrochemical response of these electrodes.[21] Interest in CNT electrocatalytic activity arises from the possibility of enhanced signal-to-noise ratio, higher voltammetric peak current and higher sensitivity for analytical applications. In addition to these effects, several studies suggest the contribution of the presence of metals (catalysts present in CNTs) in the electrochemical response of the electrodes.[22,23] While conducting studies on the reduction of the peroxide group (cumene hydroperoxide and tert-butyl hydroperoxide) with nanotubes on printed electrodes, Stuart et al.[24] confirmed the Compton's group initial studies on the response of electrocatalytic particles of the residual catalyst. These studies show a catalytic reduction of specific analytes that are very sensitive to Fe nanoparticles.

Motivated by the possible catalyst interference in the electrochemical response of the nanotubes, Jones et al.[25] studied the response of HOPG electrodes modified by catalyst-free CNTs. At least relative to the ferri/ferrocyanide system, the study revealed that the electrodes were reversible and the peak current obtained was proportional to the amount of tubes. According to the authors, this response demonstrates the non-interference of the catalyst in the response of the nanotube probe ($\Delta E_p \sim 60$ mV) and the contribution of the amount of CNTs to the peak current of the electrode. The authors also observed that the same electrode modified with "Bamboo like" nanotubes features 66 mV peak separation.

Recently some studies reported a greater interference from the catalysts and impurities in CNT electrode electrochemical response for the detection of organic molecules. The association follows naturally from historical participation of metals in electrochemical reactions.[26] In parallel to the analysis of CNT responses, there was a comparison study on structural and morphological effects upon the electrochemical response of HOPG and CNTs. Figure 2 shows the analogy used to explain the CNT and HOPG electrochemical responses.[19] The sides of the basal plane of graphite are equivalent to the edges of the overlapping graphene planes. Similarly, the ends of the nanotube tips correspond to graphene edges, with the difference that each tube corresponds to a graphene sheet.

(a) **Basal-plane**

Edge-plane

(b) **Basal-plane**
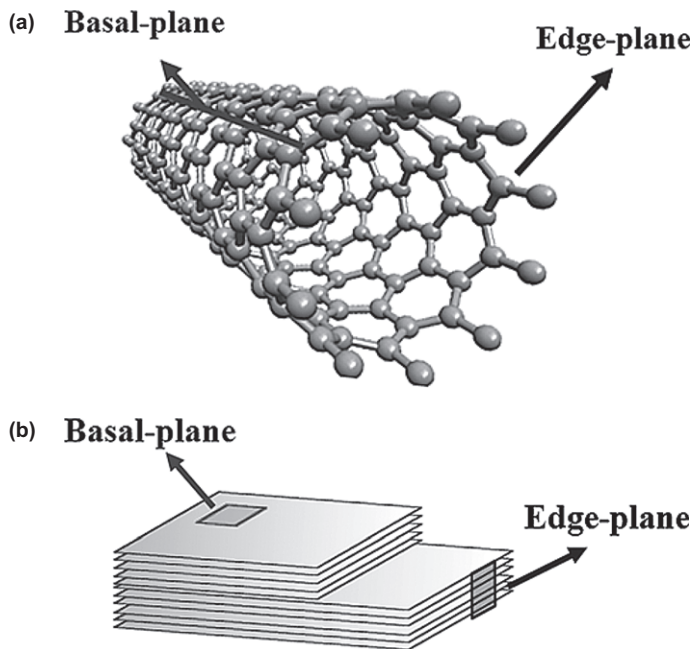
Edge-plane

Fig. 2 Schematic drawing of the basal-plane and edge-plane of (a) HOPG and (b) CNT (adapted from ref. 29).

In this context, Lai *et al.*[27] give definitive evidence for fast electron transfer at pristine HOPG electrodes using high resolution electrochemical microscopy. They locally discriminated the electrochemical contribution by the basal or edges planes of the nanotubes using 2 different redox couples: potassium ferri/ferrocyanide and hexaammineruthenium (II/III) chloride ($[Ru(NH_3)_6]Cl_2/[Ru(NH_3)_6]Cl_3$) in 0.1 mol L^{-1} KCl, as supporting electrolytes. A similar study with a single MWCNT[28] and the hexaammineruthenium couple obtained k^0 values < 0.1 cm s^{-1}. Because of a large scattering of data suggesting MWCNT react *via* inhomogeneous active sites, the authors suggested defects contribute to CNT electrochemical reactivity.

As previously mentioned, the processing history of carbonaceous material electrodes (number of defects, functionalisation, degree of oxidation, and so on) affects their respective electrochemical response. Regarding CNT functionalisation, several studies indicate a very positive effect on their electrochemical response.[30,31] The intrinsic properties of the CNTs, such as chemical stability, high electrical conductivity, high surface area, among other things, promote electron exchange between the solid and liquid reagents. Several modifications have been carried out on CNT surfaces, such as addition of DNA molecules,[32,33] polymers (such as polypyrrole[34] and blue polymethylene,[35] poly-(urea formaldehyde),[36] *etc.*), proteins,[37,38] enzymes,[39,40] organic molecules,[41] *etc.*

In a study evaluating the change in CNT electrochemical response after functionalisation with oxygenated groups, Chou *et al.*[42] confirmed the improvement in the electrode response using the redox probe

ferri/ferrocyanide with $KCl_{(aq.)}$ as supporting electrolyte. Additionally, this study showed that the nanotubes dispersed on an Au electrode gave an ΔE_p of 105 mV whilst an aligned CNT electrode gave an ΔE_p of 72 mV (as control, a Au electrode without the CNTs gave an ΔE_p of 92 mV).

Crevillen et al.[43] evaluated the response of CNTs functionalised by oxidative acids. They showed good response for bioactive molecules such as vanillin, pyridoxine, maltol, (+)-catechin, ascorbic acid, dopamine and others. A similar response to functionalised graphite in this study suggested non-interference from metal catalysts (left over from CNT synthesis). In this sense, the authors related the electrochemical response with enendiol group terminations. Finally, the authors speculate that these groups reactive with the aforementioned molecules resulting from the interaction mechanism between oxygen-containing species present on the surface and enediol groups (hydrogen bond).

The electron transfer process between the electrode and the solution can be described by the theory of Marcus–Gerischer.[44–46] As in the Marcus model, the electron transfer process in the Gerischer model requires energy corresponding to the reorganization between the oxidized and reduced states. However, this step requires more time in solution than in the solid state due to the reorganization of the solvation shell. In this regard, it is noteworthy that the Fermi level position in the electrode depends on the potential imposed, and the electron transfer occurs when the Fermi level of the species in solution and of the electrode have the same value. Although some conceptions assume that the absence of states near the Fermi level would result in lower charge transfer, the study conducted by Heller et al.[47] revealed that in semiconductor nanotubes electrochemical current occurs even with this absence. According to this theory, in MWCNT the proximity of the walls results in superimposition of states and thus it is easier to transfer electrons between the ions in solution and the solid.[48] In other work, Heller et al.[47] shows the density of states of a single-walled nanotube interface in a solution, which emphasises the charge transfer between the states of the redox couple and the states of the redox species. The large number of states in the CNT promotes an increase in the electron transfer between the redox species and nanotube.

3 Synthesis and characterisation of VACNT

Vertically aligned CNTs are usually grown using Chemical Vapor Deposition (CVD), which involves the catalytic decomposition of a carbon-containing gas above a surface covered in solid catalytic nanoparticles of a transition metal.[7] VACNT have been prepared by several types of CVD activation sources, such as plasma enhanced, microwave plasma, hot-filament, and fluidized bed, and on wide range of substrates. Before VACNT growth, metallic substrates need to be covered by a barrier layer, which is normally oxides or silicon, to avoid carbon diffusion into the bulk during growth. In addition, a thin

(few nm) catalytic layer of the chosen transition metal (typically iron or nickel) needs to be deposited on the substrate, usually by evaporation or sputtering. This catalytic layer is then heated under a hydrogen/nitrogen atmosphere inside a reactor chamber, causing the layer to melt and ball-up into isolated nanoclusters under surface tension. The size and separation of the nanoclusters depends upon the thickness of the catalyst layer and heating conditions (temperature and duration). Each individual nanocluster becomes the catalyst for the growth of one CNT, and so the size and separation of these nanoclusters defines the diameter and areal density of the resulting CNTs. A gaseous carbon source is then introduced at the correct temperature for CNT growth, normally for a short period of time. CNTs grow in random directions and intertwine like spaghetti, with a typical entangled structure. If the density is high enough the CNT grow vertically aligned due to competition for space, forming VACNT forests. Often a DC bias is applied to ensure the CNTs grow vertically upwards independently of the areal density.

Although the literature has hundreds of papers that describe CVD methods to grow vertically aligned SWCNT or MWCNT and hundreds more papers discussing their electrochemical properties, it is quite rare to find publications that present both the synthesis and electrochemical characterisation together. In the next section, we will present the literature and our developments on this topic.

3.1 Literature

One of the first reports of alignment of carbon nanotubes on large areas was by Li et al.[49] using thermal deposition of hydrocarbons. In this work, mesoporous silica was the substrate. A silica network with relatively uniform pores was obtained, having iron oxide nanoparticles embedded in the pores. The iron oxide nanoparticles were then reduced at 550 °C in 180 Torr of flowing 9% H_2/N_2 (110 cm^3 min^{-1}) for 5 h. The nanotubes grew along the direction of the pores causing mis-orientation of nanotubes in some cases. The alignment was due to the constraint of the vertically aligned pores.[50]

To the best of our knowledge, Gao et al.[51] were one of the first groups that reported the growth of VACNT material and their application in electroanalysis. These authors prepared VACNT by pyrolysis of iron (II) phthalocyanine, $FeC_{32}N_8H_{16}$ (known as FePc), which contains both the metal catalyst and carbon source required for the nanotube growth. The pyrolysis of FePc was performed under Ar/H_2 at 800–1100 °C in a flow reactor consisting of a quartz tube and a dual furnace fitted with independent temperature controllers. The resulting carbon nanotubes appeared on the quartz plate substrate as a black layer, which could be scraped off from the substrate as powder or freestanding film. The authors reported that the freestanding films combined with a conducting polymer formed an outstanding biosensor. In this work, the researchers highlighted the usefulness of the polypyrrole-based glucose oxidase

system for detection of glucose. The use of these three-dimensional CNT electrodes offers advantages in that they offer high sensitivity, and that large accessible enzyme loadings can be obtained within an ultrathin layer.

Okuno et al.[52] were one of the first groups to grow VACNT material and applied it as electrochemical sensors. A p-type Si wafer was thermally oxidized to form an SiO_2 film (150 nm). SWCNT were synthesized by thermal CVD using $Fe(NO_3)_3.9H_2O$, $MoO_2(acac)_2$ and alumina nanoparticles in the liquid phase. Then, the substrate was heated up to 900 °C in Ar atmosphere, and then ethanol vapor was supplied for 10 min. The authors reported the formation of a microelectrode chip directly on Pt surfaces. The electrochemical characteristics of the devices were investigated using $K_3[Fe(CN)_6]$ in connection with cyclic voltammetry and showed fast charge transfer. The electrochemical signals of electroactive amino acids; L-Tyrosine, L-Cysteine and L-Tryptophan were detected using differential pulse voltammetry (DPV) showing very low limits of detection.

Tsierkezos et al.[53] prepared VACNT with an outer diameter ~ 4.0 nm selectively on SiO_2 using a thermal CVD feed of either acetonitrile or benzene as carbon sources, with ferrocene ($FeCp_2$) as catalyst. The $FeCp_2$ solution was introduced to the furnace through a syringe with a flow rate of 0.2 mL min^{-1} at a temperature of 900 °C. The synthesis process was performed using argon as carrier gas. The extracted CV and Electrochemical Impedance Spectroscopy (EIS) results were critically compared with those obtained using a glassy carbon electrode (GCE).

Gong et al.[54] produced on a SiO_2/Si wafer, 'super' long (5 mm) vertically aligned double-walled carbon nanotubes by water-assisted CVD of high-purity (99.99%) ethylene in the presence of an Fe catalyst with helium/H_2 (2.5 : 1 v/v) as a carrier gas under 1 atm pressure at 700 °C. The authors report that they have demonstrated experimentally the effects of the nanotube tip and sidewall in CNT electrodes, and the effects of their oxidation states on the electrochemistry of various commonly used electrochemical probes, such as $K_3[Fe(CN)_6]$, nicotinamide adenine dinucleotide (reduced) (NADH), cysteine, H_2O_2, oxygen and ascorbic acid. Through using super long VACNT electrodes, they set experiments to expose only the sidewall or tip(s) of the CNTs. The authors concluded that the electrochemistry at carbon nanotube electrodes is not always facilitated by the nanotube tip and/or oxygen-containing surface groups. In fact, the relative electrosensitivity to the nanotube tip and sidewall and their oxidation states varies with different electrochemical probes and relates to distinct reaction mechanisms.

More recently, open-ended VACNT arrays were synthesized by a water-assisted CVD process.[55] The growth was on the (0 0 1) surface of silicon with a silicon oxide layer. A 15-nm-thick Al_2O_3 layer and a 2-nm-thick Fe layer were deposited onto the silicon surface by sequential electron-beam evaporation. The CVD process was carried out in a Lindberg Blue tube furnace, with ethylene (150 sccm) as the carbon source, hydrogen (200 sccm) and argon (350 sccm) as the carrier gases. A trace amount of water

was introduced into the CVD chamber by controlled bubbling of a small amount of argon through water. After the ethylene flow was shut off, the water, argon and hydrogen flows were maintained for 5 min until the CVD process was shut down. The authors transferred the well-aligned, high-purity, open-ended CNT membrane onto the surface of glassy carbon electrodes using Nafion. The electrochemical voltammetric performance of CNT/Nafion/GCE was studied for the determination of dopamine in terms of stability, sensitivity and detectability.

In all those experimental procedures, the authors reported a fast charge-transport rate at the electrode/electrolyte interface, which is desirable for electroanalytical applications. However, as we present in the next section, slight changes in the experimental growth procedure can produce very different materials.

3.2 Our developments

3.2.1 VACNT growth. VACNT films have been grown on titanium grade 2 substrate (pure titanium) or titanium grade 5 (Ti6Al4V alloy) by microwave plasma assisted chemical vapor deposition (MWCVD).[56–58] Figure 3 shows a schematic drawing of the MWCVD reactor. The home-built MWCVD reactor chamber, shown in Fig. 3a, has a 108 mm-diameter TEM01 cylindrical cavity with a 1 kW magnetron directly coupled to a cylindrical coupler. The cavity is separated from the coupler by a 100 mm-diameter quartz window. The water-cooled chamber
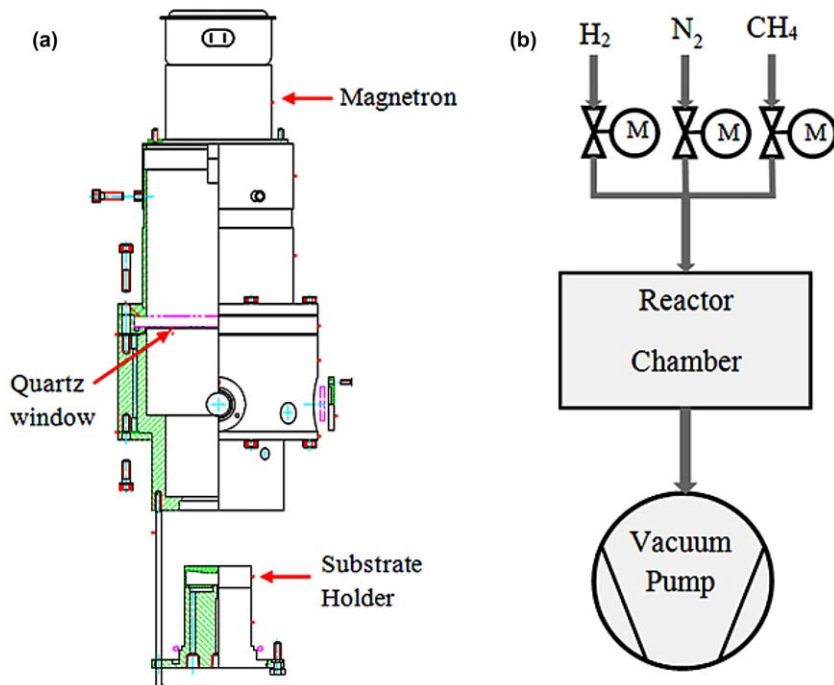
Fig. 3 Schematic representation of MWCVD reactor: (a) Schematic drawing of the MWCVD reactor chamber; (b) Schematic diagram of the reactor setup.

was made from aluminium and was internally anodized to avoid corrosion by harsh environments. The substrate holder forms a microwave trap to concentrate the plasma hemisphere directly above it. The substrate holder has a diameter of 50 mm and its temperature is further controlled by resistive heating underneath. Figure 3b shows the three gases (H_2, N_2 and CH_4) mixed by mass flow controllers, that flow into the MWCVD reactor chamber while the chamber pressure is maintained by a rotary vacuum pump.

Initially, the titanium substrate was cleaned and placed in an oven at 480 °C in air to form a titanium oxynitride layer that acts as a diffusion barrier for the metal catalyst (Fe, Ni, Co, Mo or alloys). The metal catalyst was then deposited either by electron-beam evaporation of a 10 nm film of (Ni or Fe) or by immersion in ethanolic solution of metal (Fe, Ni or Co) nitrate. Before growth, the substrates are exposed to a plasma of N_2 (20 sccm) and H_2 (80 sccm) at 30 Torr for 5 minutes after the substrate reaches 760 °C. VACNT growth then proceeds by adding CH_4 (14 sccm) to the N_2/H_2 gas mixture. The growth of VACNT was performed for 2 minutes at 30 Torr and 760 °C, with temperature measured on the backside of the substrate.

The procedure for ending the growth process was critical and provided two different materials of interest for electrochemical applications. The first method (called GE-1) ended CNT growth by simply turning off the methane flow 30 seconds before turning off the microwave power and substrate holder heater. This resulted in VACNT with mostly nanotube tips on the top surface. The second method (called GE-2) ended growth by turning off the microwave power 30 seconds before turning off the methane flow. In this case, nanotube growth continues at a slower rate, but the CNTs lose vertical alignment resulting in a high density of entangled nanotubes on the top surface. In both cases the N_2/H_2 gas mixture flow and gas pressure in the reactor are maintained upon cooling to room temperature. Then samples were removed from the MWCVD reactor for further processing.

3.2.2 Functionalisation of VACNT. Nanotube functionalisation and exfoliation were performed in a much less powerful pulsed DC plasma reactor.[59,60] The chamber walls form the anode, while the CNT samples were placed over the substrate holder cathode. The reactor chamber was first evacuated to 10^{-5} Torr by a diffusion pump to ensure low residual air. Then pure oxygen (1 sccm) was introduced and the chamber pressure was controlled at 80 mTorr. The pulsed DC power supply was set at −700 V at 20 kHz and 45% duty cycle. Treatments were accomplished within 2 minutes.

The result was a heavily oxidized CNT surface with extensive exfoliation. These conditions were optimal for exfoliation since lower oxygen concentrations and pressures led only to functionalisation, while higher pressures and longer treatment times led to nanotube erosion. Considering that nanotubes are exfoliated in an oxygen atmosphere, the graphene sheets exposed upon exfoliation are graphene oxide (GO). Hence, the resulting samples are named VACNT-GO.

3.2.3 Characterisation of VACNT. Ramos[59,61] demonstrated that CO_2 laser etching of functionalized VACNT gradually re-stablishes the wetting properties of pristine VACNT, depending on laser irradiance. This enabled VACNT to be made with controlled wetting properties, ranging from superhydrophobic to superhydrophilic. To evaluate the surface energy of as-grown, functionalised and laser-treated VACNT films, the contact angle (CA) was measured by a Krüss Easy Drop system using the sessile drop method at room temperature. Di-iodomethane, polyethlene glycol, glycerol, and deionised water were used to estimate surface energy. The liquid drop (2–4 μL) was placed onto the VACNT surface with a microsyringe. The drop image was recorded by video camera and digitised. The surface energy (γ), as well its dispersive (γ_d) and polar (γ_p) parts, were calculated by the Owens and Wendt method.[61,62]

Raman Scattering Spectroscopy (Renishaw 2000 system), with an Ar^+-ion laser ($\lambda = 514.5$ nm) in backscattering geometry, was used to investigate structural modifications of samples. The Raman shift was calibrated for the diamond peak at 1332 cm^{-1}. All measurements were carried out in air at room temperature.

To assess the chemical modification promoted by each treatment, the samples were analysed in place by X-ray photoelectron spectroscopy (XPS), using the $AlK\alpha$ line with a VG CLAMP hemispherical analyser. The inelastic scattering background of the C 1s, and O 1s electron core-level spectra were subtracted using Shirley's method. All binding energies (BE) were referenced to C 1s at 284.5 eV. The assignment of peak locations and corresponding fitting of XPS spectra were performed with curve fitting and data analysis software Fityk 0.9.2.[63]

3.2.3.1 Surface energy of VACNT films. Figure 4 shows the surface morphology of a VACNT sample under study. VACNT films were grown roughly aligned perpendicularly to the substrate, as shown in the SEM micrographs. A dense forest of aligned nanotubes is formed (Fig. 4(a)), where the CNT separation is optimized by van-der-Waals interactions among the tube tips. Figure 4(b) shows a high resolution TEM image of the carbon nanotubes, showing that they are multi-walled with a bamboo-like structure. Figure 4(c) and (d) show the different morphologies obtained on a VACNT surface after wetting with deionised water as a result of surface treatment. Figure 4(c) shows the morphology after wetting the as-grown VACNT. The as grown VACNT surface is hydrophobic. This is a quite typical morphology shown in many wetting studies of VACNT.[64] The VACNT are bent and their tips are joined forming irregular shapes on a micrometer scale. These microstructures are irregular shapes and their formation is explained in literature by a partial wetting with bending caused by forces generated during slow water evaporation.[61] The wetting after oxygen plasma treatment of GE-1 growth ending is quite similar to the as grown one despite being hydrophilic.

Contact angle (CA) measurements with deionized water were used to evaluate wetting and measure surface energies. Figure 5 shows photographs of water droplets on each of the surfaces of the VACNT films
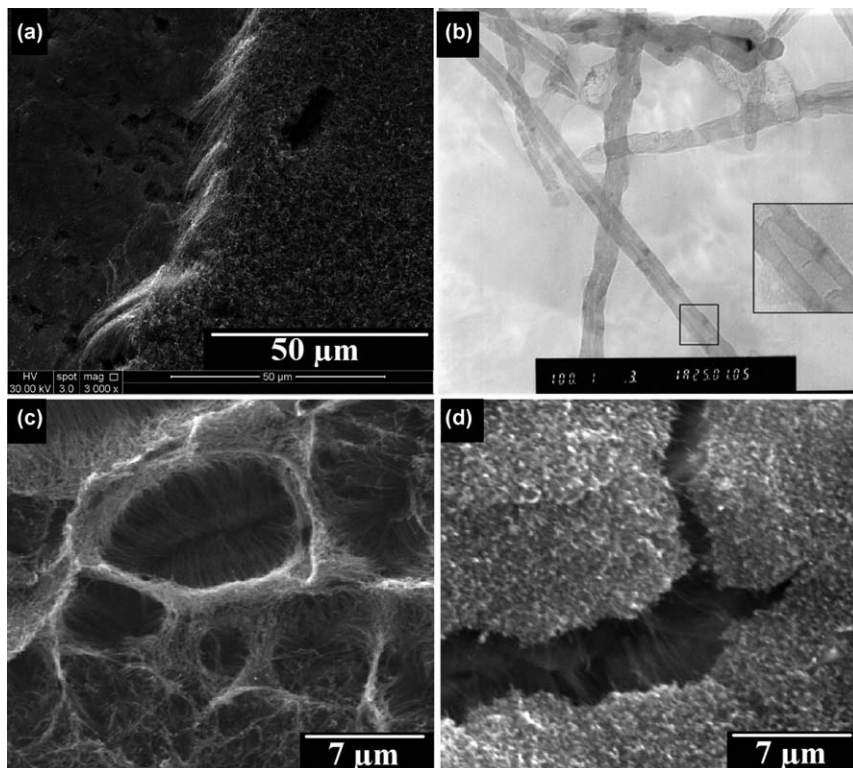
Fig. 4 (a) SEM micrograph of as-grown VACNT surface; (b) high resolution TEM image of as-grown VACNT (the inset shows the cross section with vertically aligned nanotubes); (c) surface of as-grown VACNT after wetting; (d) surface of oxygen-plasma-treated CNTs (VACNT-GO). The typical morphology obtained after wetting the samples with GE-2 growth ending submitted to O_2 plasma treatment is shown in Fig. 4d. Some structures like cracks were observed but most of the surface tips were unchanged. The VACNT surface obtained after O_2 plasma treatment, despite the growth ending method, became super-hydrophilic and was completely wetted by DI water.

analysed. As observed, the CA measured on as-grown VACNT was $\sim 144 \pm 6^\circ$ (Fig. 5(a)), whilst after oxygen-plasma etching CA was virtually zero (Fig. 5(b)). The large decrease of CA with plasma etching is due to attachment of oxygen-containing groups, such as (–C=O, –COOH),[61] which promote a chemical modification on the nanotube surface, inducing a transition from hydrophobic to super-hydrophilic characteristics. CNT surface oxidation by oxygen-based plasma treatment is already known, as shown by the FTIR and TFD data of Naseh et al.,[65] and by Tzeng et al.[66]

A complete wettability study of the VACNT surfaces was performed by CA measurement. The liquids previously mentioned were used as probes, and surface energies were calculated by the Owens and Wendt method.[62] A complete description of these measurements and method may be found elsewhere.[67] Remarkably, there is a huge increase in the polar contribution to the surface energy after the oxygen plasma treatment. These measurements show clearly that the grafting of polar groups by the O_2 plasma efficiently changes the polar part of the surface energy.
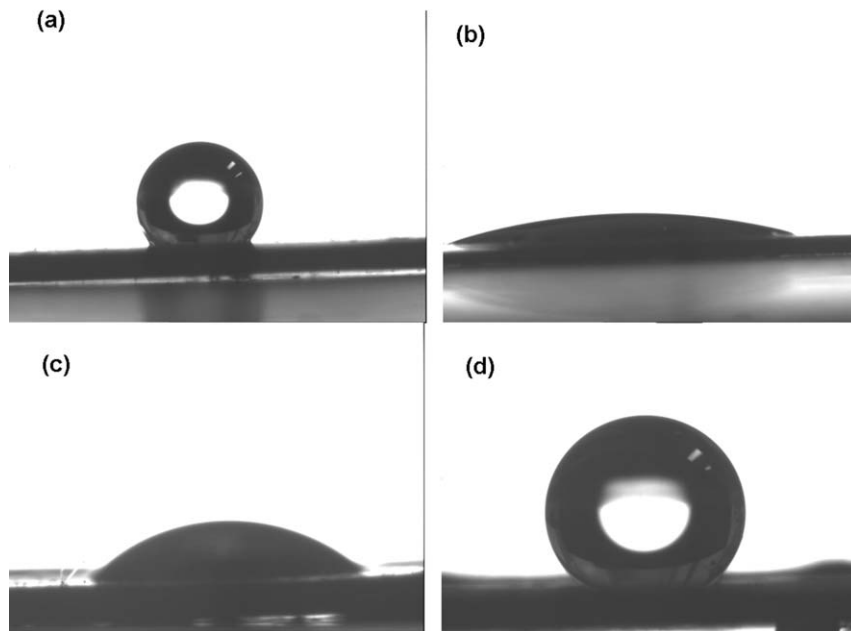
Fig. 5 Photographs of water droplets on (a) as-grown (b) after oxygen plasma etching, (c) after oxygen plasma etching and CO_2 laser irradiance -35 kW cm^{-2}, and (d) after oxygen plasma etching and CO_2 laser irradiance -50 kW cm^{-2} VACNT films (adapted from ref. 67).

This change is responsible for the change from a super-hydrophobic to a super-hydrophilic character. We performed controlled laser irradiation experiments to partially remove the effects of oxygen plasma. CO_2 laser irradiation of these CNTs at 15, 25, 35 and 50 kW cm^{-2} produced a gradual decrease of the polar part of the surface energy, restoring the original CA value of the as-grown VACNT, which restored the super-hydrophobic character.

3.2.3.2 XPS analysis. XPS analysis is fundamental to determine surface chemical composition. Figure 6 shows the C 1s fitted photo-emission spectra recorded after exposure of the VACNT sample to the oxygen plasma and CO_2 laser irradiance, as detailed above. The C 1s curve of the as-grown VACNT (Fig. 6 (a)) was deconvoluted into six peaks at 284.7, 285.5, 286.6, 287.5, 289.2 eV and 291.3 eV.[68] Each peak corresponds to aliphatic carbons (C–C), carbon atoms with C–O, C–O–C, or C–OH single bonds, carbon atoms with C=O double bonds, and –COO, respectively. The last peak at 291.3 eV has been attributed to the 'shake-up' peak (π–π* transitions).

After exposure to the O_2 plasma, the main peaks at 286.6, 287.9, 289.4 eV showed a significant increase in area (Fig. 6 (b)). This implies the formation of strong C–O bonds, mainly carboxyl groups. Further investigation of the effects of CO_2 laser irradiance on oxygen-plasma-treated VACNT was also evaluated. The deconvolution of the C 1s spectra (Fig. 6(c)) on samples exposed to 50 kW cm^{-1} laser irradiance showed
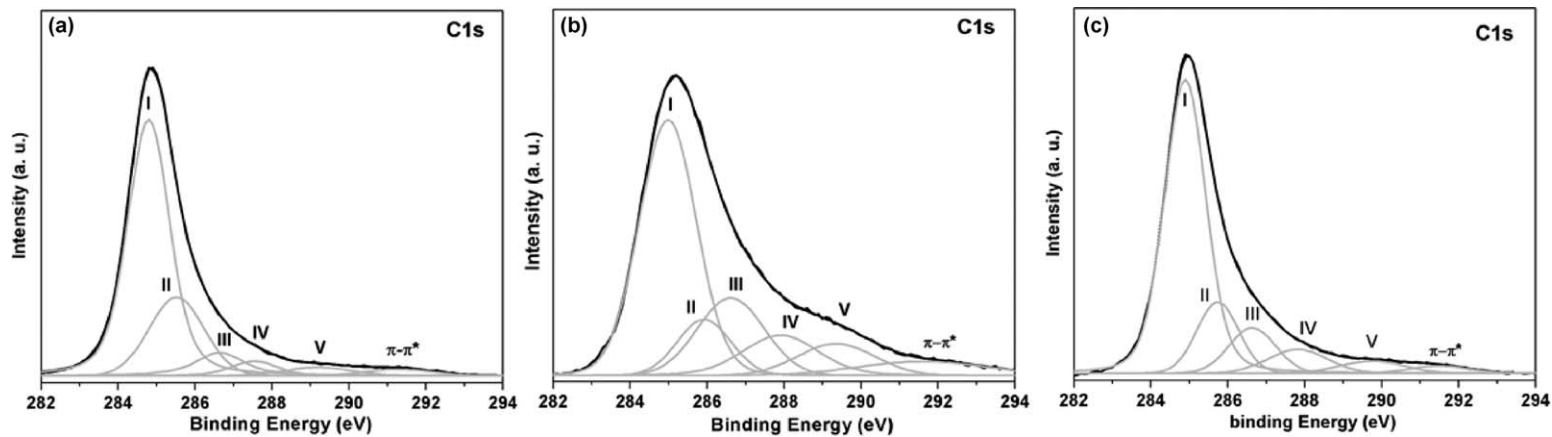
Fig. 6 XPS C 1s peaks of VACNT **(a)** as–grown, **(b)** treated with oxygen plasma and **(c)** CO_2 laser irradiance at 50 kW cm^{-2}.
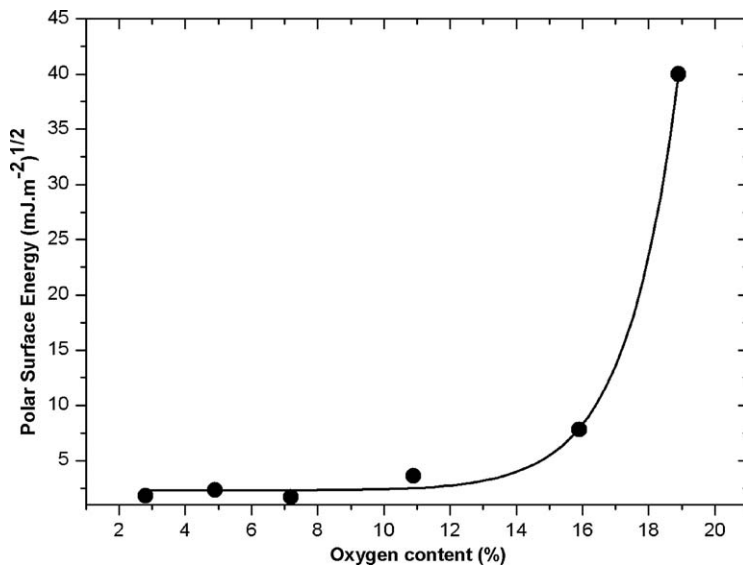
Fig. 7 Correlation between polar surface energy with percentage of oxygen on sample surface as analysed by XPS.

its restoration compared to Fig. 6(a). Because CO_2 laser etching evaporates only superficial parts of the nanotubes, it is clear that the O_2 plasma treatment only affects the surface, and has a limited depth. The recovery of wetting characteristics and XPS results to those of as-grown nanotubes indicate that nanotubes keep their core structure underneath the O_2 plasma-treated surface.

Indeed, the oxygen plasma technique promotes a heavy grafting of oxygen species on surface. The percentage of carbon and oxygen on the sample surface, as measured from XPS analysis, varied from 97 and 3%, respectively, on as-grown samples, to 78 and 19%, respectively, after O_2 plasma etching. The subsequent CO_2 laser technique effectively removes these grafted oxygen species from the surface.

A further correlation is demonstrated in Fig. 7 by plotting the polar surface energy as a function of percentage of oxygen on corresponding sample surface, as measured by XPS. The variation of the polar part of surface energy is impressive, fitting neatly ($R = 0.9984$) to an exponential growth dependence on oxygen coverage. Figure 7 clearly shows that the surface energy of VACNT and, consequently, their wetting behaviour, are correlated to the coverage of polar groups on surface. Some studies have already shown, by various methods, variation of surface energy for VACNT surface functionalisation, but none have shown such a huge variation and such a precise wetting control. A likely reason it was observed is due to a very effective functionalisation obtained by O_2 plasma, which grafted 18.9% oxygen onto the VACNT surface.

3.2.3.3 *High resolution scanning electron microscopy.* Figure 8 shows typical higher resolution SEM images of the VACNT surfaces obtained by turning the microwave power off before turning off the methane
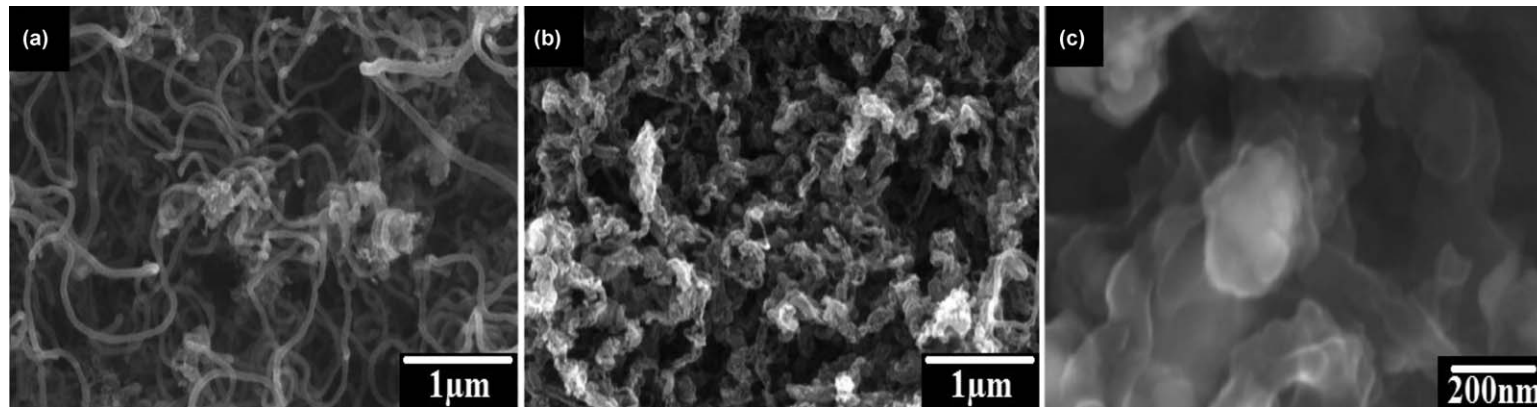
Fig. 8 High resolution SEM images of VACNT resulting from ending film growth by turning the microwave power off before turning off the methane flow. **(a)** The as-grown entangled carbon nanotubes on surface; **(b)** the oxygen-plasma etched surface; **(c)** further magnification of the oxygen-plasma etched surface showing overall exfoliation of surface carbon nanotubes.

flow when ending the growth process (GE-2). Figure 8(a) shows that the as-grown samples have an entangled structure, not only at the VACNT tips but also with extended regions of their lateral surface. This surface has been attacked by the oxygen plasma, as shown in Fig. 8(b). Clearly, the same entangled structure persists but the nanotubes walls are severely damaged. Further magnification is shown in Fig. 8(c), showing that the damaged nanotubes on the surface were exfoliated, showing their graphene sheets petal-like around the nanotube core.

Figure 9 shows typical higher resolution SEM images of the VACNT surfaces obtained by turning the methane flow off before turning off the microwave power when ending the growth process (GE-1). Figure 9(a) shows that in this case the CNTs remain roughly aligned. The O_2-plasma etching in this case attacks mainly the CNT tips, as shown by the top view in Fig. 9(b). Further magnification of one of these tips (shown as white spots in Fig. 9(b)) is shown in Fig. 9(c). A clear tip exfoliation is shown.

3.2.3.4 Raman spectra. Figure 10 shows first-order Raman scattering spectra of VACNT films, for the as-grown (Fig. 10(a, c)) and the oxygen-plasma-treated (Fig. 10(b, d)) samples, for both growth ending procedures GE-1 and GE-2. These spectra show a difference in their D and G bands.[69] The main analysis is of the peak around $1350 \, \text{cm}^{-1}$ (D-band), assigned to the carbon disorder-induced, and the band at $1582 \, \text{cm}^{-1}$ (G-band) resulting from in-plane vibrations of ordered graphite.[70–72] The deconvolution of the spectra of Fig. 10(a) and (c) were performed with Lorentzian shapes for the D and G bands, and a Gaussian shape for the D′ peak, as used by other authors. For the curve fitting of Fig. 10(b) and (d), the Gaussian peaks around 1450–$1525 \, \text{cm}^{-1}$ and around $1250 \, \text{cm}^{-1}$ were also included, because it was necessary for the fitting. The band around 1450–$1525 \, \text{cm}^{-1}$ has already been observed previously for heavily functionalised MWCNT. The shoulder at $1250 \, \text{cm}^{-1}$ has its origin in a double-resonance process on graphene phonon dispersion curves. Despite these new bands being present, whose origin is due to the grafting of the polar groups onto the MWCNT surface, the following analysis is based only on the changes in the D and G bands. The changes in the D-band can be used for exploring structural modifications of the nanotube walls owing to introduction of defects and attachment of different chemical species.[69,71] Also, the D′ band carries information about disorder in the sp^2 lattice. Based on the fitting parameters, the full width at half maximum (FWHM) and the ratio of the integrated areas under the D and G bands (I_D/I_G) are summarized in Table 1.

The integrated intensity ratio of the D and G peaks (I_D/I_G) has been often used as an indication of the level of chemical functionalisation or defect density on carbon nanotube surfaces.[69] This ratio is much larger ($I_D/I_G = 1.6$) for GE-2 compared to GE-1 ($I_D/I_G = 0.54$), indicating a more defective surface for GE-2. For GE-1 the I_D/I_G ratio increases from 0.54 to 0.7 upon O_2 plasma etching, indicating that the defect density increases. This increase in defect density is also shown by G line broadening. For GE-2 the I_D/I_G ratio reduces from 1.6 to 1.2, which gives the false idea of a
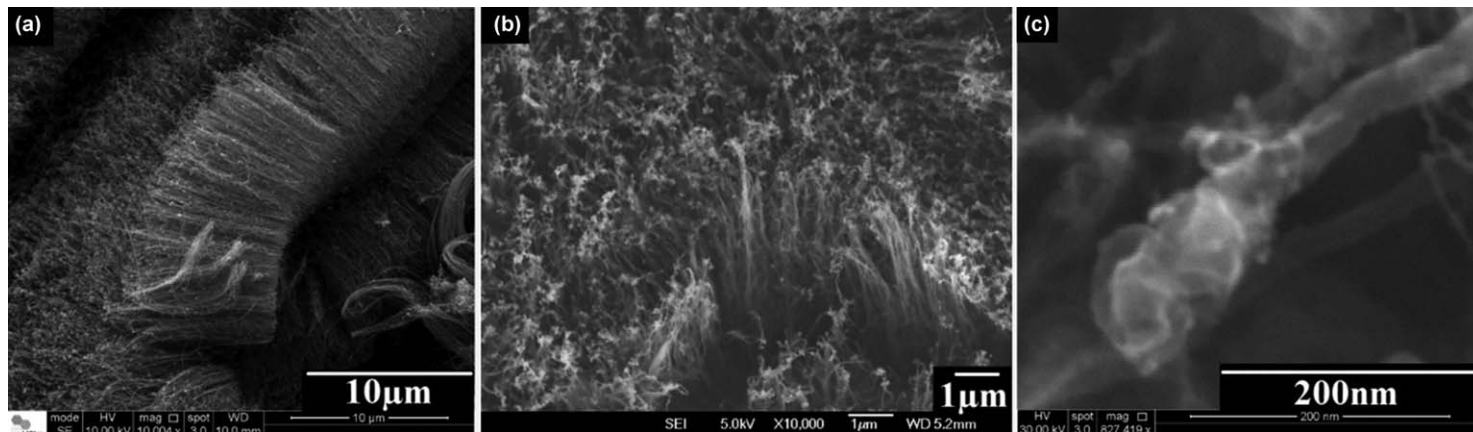
Fig. 9 SEM micrographs of O_2-plasma-treated VACNT samples showing (a) parallel alignment; (b) top view, and (c) tip exfoliation (Adapted from references 60 and 80).
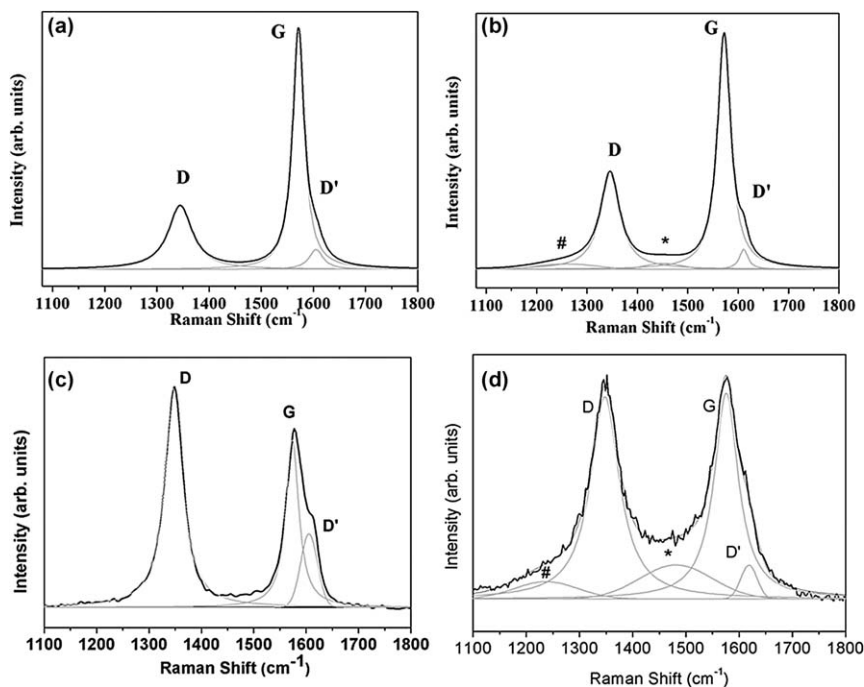
Fig. 10 Deconvolution of D and G bands at 514.5 nm for VACNT under study: (a) GE-1 as-grown, (b) GE-1 after oxygen plasma (c) GE-2 as-grown, (d) GE-2 after oxygen plasma. The symbol # indicates a band close to 1250 cm^{-1} and the symbol * indicates a band close to 1480 cm^{-1}.

Table 1 Summary of D and G band analysis.

Sample under study	D-band position (cm^{-1})	G-band position (cm^{-1})	I_D/I_G	FWHM (D)	FWHM (G)
As-grown GE-1	1344.8	1571.3	0.54	56.3	27.4
O$_2$ plasma etching GE-1	1345.1	1572.1	0.7	54.1	32.3
As-grown GE-2	1348.4	1577.8	1.6	42.0	35.8
O$_2$ plasma etching GE-2	1347.6	1575.7	1.2	66.0	55.3

reduction in defect density for the O$_2$-plasma-treated sample. However, the spectrum is influenced by a huge broadening of the D and G bands and the large intensities of the new bands close to 1250 and 1480 cm^{-1}.

In conclusion, GE-2 samples are much more defective than the GE-1 ones. Consequently, their structural modification upon O$_2$-plasma treatment is more intense, as shown by the higher intensities of the new bands close to 1250 and 1480 cm^{-1} and, also, by the D and G band line broadening.

4 Electrochemical (bio)sensors based on VACNT

Based in the improvement of the electrochemical behavior of VACNT electrodes, the use of VACNT as an electrodic material for the establishment of novel electroanalytical approaches has been explored.

The research focused upon this general goal has been performed to solve some important analytical issues involving the determination of different analytes in various sample matrices. The next sections are dedicated to the presentation and discussion of the relevant works employing VACNT electrodes in the development of novel electrochemical sensors and biosensors.

4.1 Electrochemical sensors based on VACNT

Table 2 summarizes some amperometric/voltammetric methods in which VACNT electrodes were used. As can be seen, the proposed electrochemical methods cover a number of different target analytes: pharmaceutics, neurotransmitters, endocrine disruptors and water contaminants. Moreover, VACNT electrodes have been used together with nanomaterials, which mimic the active centre of enzymes for fabrication of several biosensors.

Many of these electrochemical methods were dedicated towards the determination of pharmaceutical drugs. The electroanalytical determination of pharmaceutical drugs has been widely explored, and the methods need to present high sensitivity, especially for the determination of active ingredients in biological fluid samples. The work reported by

Table 2 Electroanalytical methods using VACNT as electrochemical sensor. LOD = limit of detection.

Target analyte (s)	Electrode	Technique	Linearity (mol L^{-1})	LOD (mol L^{-1})	Ref.
Atorvastatin calcium	VACNT-GO	DPAdASV	9.0×10^{-8}–3.81×10^{-6}	9.4×10^{-9}	80
L-cysteine	PtNPs/ MWCNT	Amperometry	1.0×10^{-6}–5.0×10^{-4}	5.0×10^{-7}	95
Dopamine	RuO$_2$/ MWCNTs	Amperometry	6.0×10^{-7}–3.6×10^{-3}	6.0×10^{-8}	92
Glucose	CuO/MWCNTs	Amperometry	2.0×10^{-4}–3.0×10^{-3}	8.0×10^{-7}	84
Glucose	CuO/MWCNTs	Amperometry	4.0×10^{-7}–1.2×10^{-3}	2.0×10^{-7}	85
Glucose	Cu nanocubes/ MWCNTs	Amperometry	5.0×10^{-4}–7.0×10^{-3}	1.0×10^{-6}	86
Glucose	NiO/MWCNTs	Amperometry	1.0×10^{-5}–7.0×10^{-3}	2.0×10^{-6}	87
Glucose	CNT/Ni	Amperometry	5.0×10^{-6}–7.0×10^{-3}	2.0×10^{-6}	88
Glucose	Ni/VACNT/G	Amperometry	5.0×10^{-4}–1.0×10^{-3}	3.0×10^{-5}	91
Hydrogen peroxide	TiO$_2$/MWCNTs	Amperometry	1.3×10^{-3}–1.5×10^{-2}	4.0×10^{-7}	93
Lead (II)	VACNT-GO	DPASV	1.0×10^{-7}–1.7×10^{-6}	4.83×10^{-12}	83
Levofloxacin	Au/ssDNA/ SWCNT	DPV	1.0×10^{-6}–1.0×10^{-5}	7.52×10^{-8}	73
Methyl parathion	AuNPs/ MWCNT	Amperometry	2.0×10^{-4}–1.8×10^{-3}	1.0×10^{-7}	95
Oxygen	Pt/VACNT-CF	Amperometry	Not reported	Not reported	96
Rutin	VACNT	DPAdASV	1.0×10^{-8}–1.0×10^{-5}	5.0×10^{-9}	76
Salbutamol	V-CNTs	CV	5.0×10^{-7}–1.0×10^{-4}	3.0×10^{-7}	74
Simvastatin	A-MWCNTs/ DHP/Ta	DPV	1.0×10^{-8}–1.0×10^{-6}	1.0×10^{-11}	79
Uric acid	AuNPs/ MWCNT	Amperometry	2.0×10^{-4}–1.8×10^{-3}	1.0×10^{-7}	94

Moraes *et al.*[73] explored the applicability of a VACNT electrode for determination of the antibiotic levofloxacin in urine samples. Levofloxacin is an antibiotic endocrine disruptor drug. Because this compound is excreted at approximately 87–90% in the unchanged and toxic form in urine, there is a growing concern about how to measure and control its concentration in the environment. For the voltammetric determination of levofloxacin, the authors employed a VACNT electrode using SWCNT previously functionalised by an acid treatment, a gold electrode as substrate and thiol-terminated single-stranded DNA (ssDNA) as orientation agent. In a comparative investigation using cyclic voltammetry (CV) and square-wave voltammetry (SWV), the Au/ssDNA/SWCNT electrode provided an irreversible levofloxacin oxidation at a lower potential of +0.81 V and a higher peak current of 2.5-fold than for a non-modified Au electrode. The authors associated these results to the electrocatalytic activity and increase in electroactive surface area of the modified Au electrode. Nevertheless, in this work, the electroactive surface area was not determined. Levofloxacin concentration was determined using SWV in the linear range from 1.0×10^{-6} to 1.0×10^{-5} mol L^{-1}, with a limit of detection of 7.52×10^{-8} mol L^{-1}. Finally, levofloxacin was determined in urine samples, with recovery percentages ranging from 98.7% and 101%, and the results were in close agreement with those obtained using an HPLC comparative method.

Another example involves the cyclic voltammetric determination of salbutamol using a VACNT electrode proposed by Karuwan *et al.*[74] The VACNT electrodes were prepared on a gold-coated silicon substrate by CVD using acetylene and argon gases at 700 °C. In this article, the authors reported an irreversible behaviour of salbutamol. Using cyclic voltammetry, the analytical curve was linear in the salbutamol concentration range from 5.0×10^{-7} to 1.0×10^{-4} mol L^{-1}, with a limit of detection of 3.0×10^{-7} mol L^{-1}. The proposed voltammetric method was efficiently applied in salbutamol determination in pharmaceutical formulations.

Rutin is a flavonoid compound found in several plants, and shows a number of interesting pharmacological actions, such as being an antioxidant, anti-inflammatory, antiallergic, antiviral and anticarcinogenic.[75] The electrochemical behaviour of this molecule was investigated using a VACNT electrode by Ye *et al.*[76] and, a differential pulse-stripping voltammetric method was established. A reversible oxidation reaction involving the transfer of two protons and two electrons was proposed for this analyte. A limit of detection of 5.0×10^{-9} mol L^{-1} was obtained under the optimized experimental conditions, and the method was subsequently applied to rutin quantification in commercial pharmaceutical products.

Pharmaceutical drugs from the statin class have also been determined using VACNT-based electrodes. The pharmaceutical class of statins includes substances of anti-lipid activity acting, therefore, in the reduction of the levels of cholesterol in blood. This activity of statins is derived from its action on the HMG-CoA reductase enzyme (3-hydroxy-3-methylglutaryl CoA reductase), which catalyses the production of mevalonic acid, the precursor of cholesterol biosynthesis.[77,78] Three papers dedicated to

voltammetric determination of statins by applying VACNT electrodes are found in the literature. In the first article, the natural statin simvastatin[79] was determined, and in the other articles, the synthetic statins atorvastatin calcium[80] and rosuvastatin calcium[81] were also determined.

Fayazfar et al.[79] proposed the modification of a highly oriented MWCNT with a dihexadecyl hydrogen phosphate (DHP) film for the improved determination of simvastatin. Recently, a composite of VACNT and graphene oxide (GO) has been successfully employed by our research group as electrode material for the determination of atorvastatin calcium in several samples, including pharmaceutical formulation and biological samples of urine and human serum.[80] The composite of VACNT and GO (VACNT-GO) was obtained by the oxygen-plasma treatment of VACNT films previously synthesized by a microwave plasma CVD method, as discussed in the previous sections. The oxygen-plasma treatment of CNT tips exfoliates the graphene foils and inserts polar oxygenated functional groups on the CNT walls, improving significantly the VACNT-GO wettability from super-hydrophobic (CA $144°$–$157°$, as-grown VACNT) to super-hydrophilic (CA $\approx 0°$, VACNT-GO). This was a crucial achievement for the application of the VACNT-GO composite as a working electrode in electroanalytical measurements. Figure 11 presents the cyclic voltammograms obtained for 5.0×10^{-5} mol L^{-1} atorvastatin calcium in 0.2 mol L^{-1} phosphate buffer solution (pH 2) containing 20% v/v methanol using the VACNT-GO electrode, and a GCE employed as "standard" carbon working electrode. The use of the VACNT-GO electrode resulted in a significant increase of the analytical signal. The quantitative analysis of atorvastatin calcium was performed using differential-pulse adsorptive anodic-stripping voltammetry (DPAdASV), in which a preconcentration step of the target analyte was performed before the differential-pulse voltammetric measurement. This strategy improved the figures of merit of the proposed method. Under the optimized experimental conditions, the analytical curve was linear in the atorvastatin calcium concentration range from 90 to 3.81×10^3 nmol L^{-1} with a limit of detection of 9.4 nmol L^{-1}. In addition, in another recent work, the VACNT-GO electrode was used for the determination of rosuvastatin calcium using square-wave adsorptive anodic-stripping voltammetry (SWAdASV).[81] The analytical curve was linear in the rosuvastatin calcium concentration range from 0.48 to 46.72 μmol L^{-1} with a limit of detection of 0.06 μmol L^{-1}.

Saito et al.[82] reported the application of a VACNT-GO electrode for the determination of lead (II). The electrode was initially evaluated by cyclic voltammetry using the electrochemical ferri/ferrocyanide redox couple. Pb(II) determination was carried out in 0.2 mol L^{-1} acetate buffer (pH 4.2) by differential-pulsed anodic-stripping voltammetry (DPASV). The deposition potential of -1.2 V applied for 300 s under magnetic bar stirring (900 rpm) forces the initial Pb(II) to adsorb onto the working electrode. The method presents high sensitivity (35.47 μA μmol^{-1} L) and low limit of detection (48.3 pmol L^{-1}). This is the lowest limit of detection reported for lead (II) using CNT or graphene electrodes. The authors attributed this high electrochemical performance to the high density of functionalised edges on CNT tips.
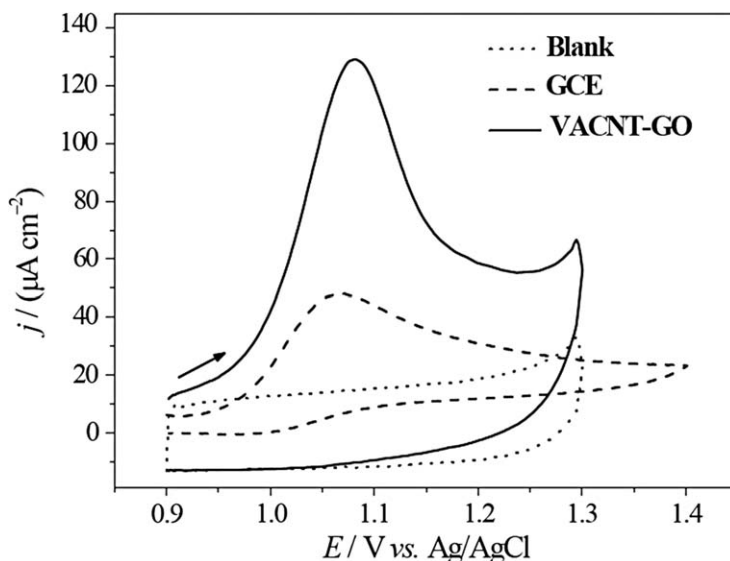
Fig. 11 Cyclic voltammograms obtained using the VACNT-GO electrode and a Glassy Carbon Electrode (GCE) in 0.2 mol L^{-1} buffer phosphate (pH$_{cond}$ 2.0, 20% (v/v) methanol) containing 5.0×10^{-5} mol L^{-1} ATOR (VACNT-GO) or 1.0×10^{-4} mol L^{-1} ATOR (GCE) (Reproduced from ref. 80 with permission from The Royal Society of Chemistry).
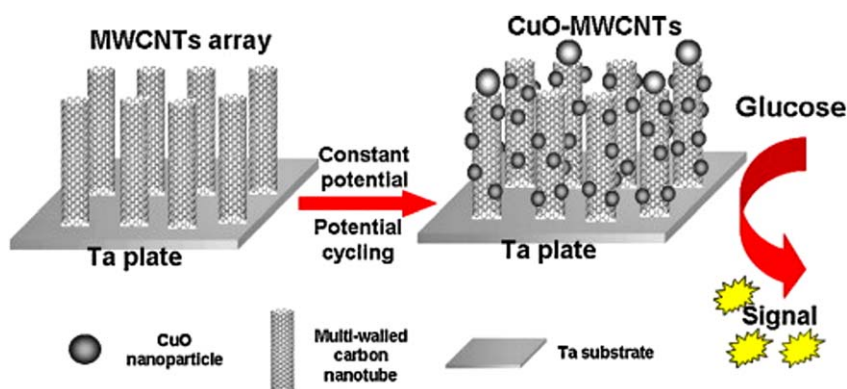
Fig. 12 A schematic diagram (not to scale) of the fabrication and application of a CuO/MWCNT glucose sensor. CuO nanoparticles are electrochemically deposited onto the MWCNT array and the resulting nanocomposite generates electrochemical signals in the presence of glucose (Reproduced from ref. 83 with permission of Elsevier).

VACNT have been used as an excellent material for incorporating several nanocatalysts in the fabrication of non-enzymatic glucose electrodes. Yang et al.[83] described the preparation of a highly sensitive non-enzymatic glucose electrode employing a vertically well-aligned multi-walled carbon nanotube array (MWCNT) grown on a Ta substrate using CVD. A schematic diagram of the fabrication of the CuO/MWCNT glucose electrode and its application is shown in Fig. 12. The experimental strategy used for the preparation of the CuO/MWCNT array sensor was as follows. As a first step, copper nanoparticles were electrochemically deposited onto the MWCNT

by applying a constant potential of 0.4 V in a 0.1 mol L^{-1} KCl solution containing 1.0×10^{-2} mol L^{-1} CuCl$_2$. In the second step, Cu nanoparticles were converted into CuO nanoparticles by cycling the potential in the range from -0.5 V to $+0.3$ V in a 0.1 mol L^{-1} NaOH solution. The amperometric responses of MWCNT array electrodes (with and without CuO modification) were obtained for successive additions of aliquots of a 0.2 mmol L^{-1} glucose stock solution and a higher response was observed for the electrode containing CuO nanoparticles (composite CuO/MWCNT). This result was explained by the characteristic electrocatalytic activity of the CuO nanoparticles towards glucose oxidation. Under the optimized conditions, the proposed CuO/MWCNT array non-enzymatic glucose sensor presented an improvement of the analytical parameters for the amperometric glucose determination compared to a number of previous related reports, in terms of higher analytical sensitivity, wider linear concentration range and lower limit of detection. The method was successfully applied for glucose determination in human-blood serum samples, with recovery percentages ranging from 94 to 100%.

For the same purpose, *i.e.*, the non-enzymatic determination of glucose, Jiang and Zhang[84] fabricated an array of CuO/MWCNT electrodes using CuO nanoparticles prepared on a MWCNT array using a magnetron sputtering deposition method. The adopted analytical steps were similar to those reported by Yang *et al.*[83] A comparison of the analytical performance obtained using these two modified electrodes revealed a slight advantage of the method using CuO nanoparticles prepared by sputtering: analytical sensitivity of 2596 µA mmol^{-1} L cm^{-2} *vs.* 2190 µA mmol^{-1} L cm^{-2} for the electrodeposited CuO; limit of detection of 0.2 µmol L^{-1} *vs.* 0.8 µmol L^{-1} for the electrodeposited CuO.

In addition to these two reports, four other results have been reported for the non-enzymatic determination of glucose using composites of VACNT and nanocatalysts. Yang *et al.*[85] prepared metallic Cu nanocubes on vertically aligned MWCNT, Zhang *et al.*[86] synthesized NiO nanoparticles on vertically aligned MWCNT by sputtering, Zhu *et al.*[87] also employed the sputtering technique to prepare Ni nanoparticles homogeneously dispersed within and on the top of a VACNT forest. More recently, Kim *et al.*[88] prepared a flexible graphite (G) foil containing Ni-coordinated vertically aligned CNTs (Ni/VACNT/G). The latter work represents an important advance in the development of VACNT-based electrochemical sensors, as it is compatible with flexible electrodes that are in the forefront of electroanalytical chemistry for portable, biocompatible and implantable sensors and biosensors.[89,90] Fig. 13(a) shows schematically the steps of preparation of the Ni/VACNT/G electrode. The flexible VACNT/G electrodes were prepared by the direct deposition of VACNT on a flexible graphite substrate using a plasma-enhanced CVD (PECVD) system. Next, the Ni nanoparticles were deposited on the VACNT/G by sputtering. Fig. 13(b) and (c) illustrate the Ni/VACNT/G electrodes and their versatility to take different forms. The electrocatalytic glucose oxidation activity on Ni/VACNT/G electrodes was tested using cyclic voltammetry assays performed in basic supporting electrolyte solutions. As can be seen in Fig. 14(a), the typical voltammetric response
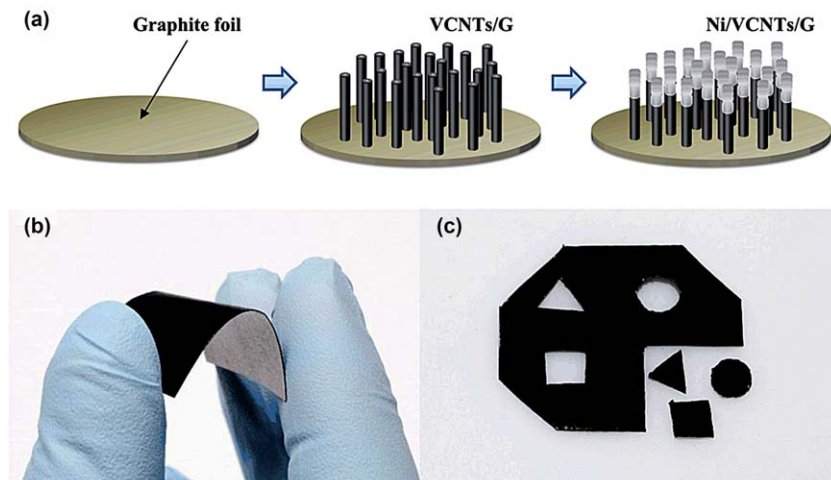
Fig. 13   (a) Schematic illustrations of the fabrication process of Ni-coordinated vertically aligned CNTs on graphite foil (Ni/VACNT/G). Photographs of (b) flexible Ni/VACNT/G and (c) various shapes of modified Ni/VACNT/G (Reproduced from ref. 88 with permission from The Royal Society of Chemistry).
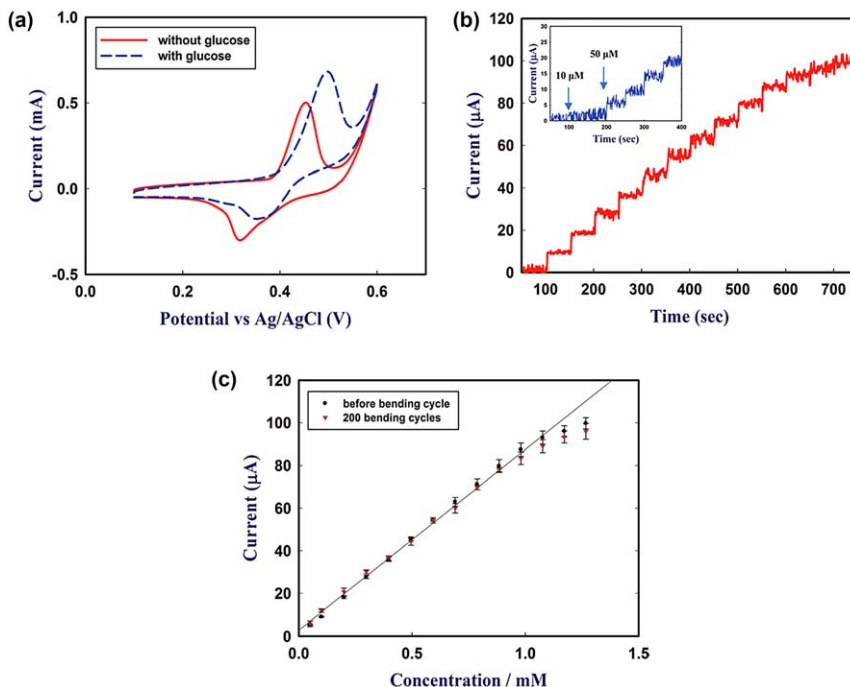
Fig. 14   (a) Cyclic voltammograms of Ni-coordinated, vertically aligned CNT electrode (Ni/VACNT/G) in 0.1 mol L^{-1} NaOH solution with and without 2 mmol L^{-1} glucose at scan rate of 50 mV s^{-1}; (b) amperometric response of the same electrode with successive addition of 0.1 mL glucose in 0.1 mol L^{-1} NaOH solution at +0.50 V (inset: amperometric response with addition of 10 and 50 mmol L^{-1}) and (c) its corresponding analytical curves before and after 200 bending cycles. (Reproduced from ref. 88 with permission from The Royal Society of Chemistry).

of the Ni/VACNT/G electrode changed in the presence of glucose; the anodic peak current increased, while the cathodic peak current decreased, and the anodic peak potential shifted in the positive direction. These experimental observations proved the excellent electrocatalytic activity of the Ni/VACNT/G electrode towards glucose oxidation, according to the following reaction schemes (Equations 1 and 2):

$$Ni(OH)_2 + OH^- \rightarrow NiO(OH) + H_2O + e^- \tag{1}$$

$$NiO(OH) + Glucose \rightarrow Ni(OH)_2 + Glucolactone \tag{2}$$
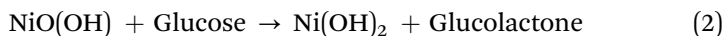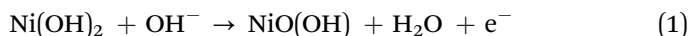
Glucose amperometric sensing using the Ni/VACNT/G electrode was evaluated before and after 200 bending cycles, in order to verify the mechanical stability of the proposed flexible sensor. The amperometric response of Ni/VACNT/G electrode for different concentration levels of glucose is showed in Fig. 14(b), and the respective analytical curves constructed before and after the 200 bending cycles are presented in Fig. 14(c). The flexible Ni/VACNT/G electrode presented a wide linearity range and limit of detection of 30 μmol L^{-1} for glucose. It maintained an amperometric response even after exhaustive cycles of mechanical stress, suggesting it may be a promising material for future applications in real clinical analysis.

In addition to the approach of incorporating nanoparticles on VACNT surfaces for the non-enzymatic determination of target analytes, by similar synthesis strategies, composites of VACNT and metallic (or metallic oxide) nanoparticles can be obtained to provide higher sensitivity in electroanalytical determinations.

Jiang and Zhang[91,92] reported the modification of vertically aligned MWCNT with TiO$_2$ or RuO$_2$ nanoparticles for the determination of hydrogen peroxide (H$_2$O$_2$) and dopamine (a neurotransmitter), respectively. In addition, VACNT modified with gold nanoparticles (AuNPs)[93,94] and platinum nanoparticles (PtNPs)[95,96] have been suggested as novel electrochemical sensors. Wang and Zhang[93] prepared vertically aligned MWCNT modified with gold nanoparticles and they tested the electrochemical performance of these composites for the determination of uric acid. The vertically aligned MWCNT were synthesised by CVD on a Ta substrate and subjected to AuNP deposition by magnetron sputtering. In Figure 15(a), the TEM image of AuNPs/MWCNT demonstrates that the nanoparticle diameter was ∼5.0 nm. Using cyclic voltammetry, this composite material showed improved electrochemical activity for uric acid oxidation, with increase of the analytical signal (anodic peak current) and negative shift of the peak potential. Finally, the amperometric response of uric acid at +0.4 V was monitored, and the response was found to be linearly dependent on uric acid concentration in the range 0.2 mmol L^{-1} to 1.8 mmol L^{-1}, with a limit of detection of 0.1 μmol L^{-1}. In another publication from the same research group, the modified AuNPs/MWCNT were investigated for the voltammetric determination of methyl parathion, a very toxic organophosphate pesticide.[94] Once again, the modified vertically aligned MWCNT electrode showed
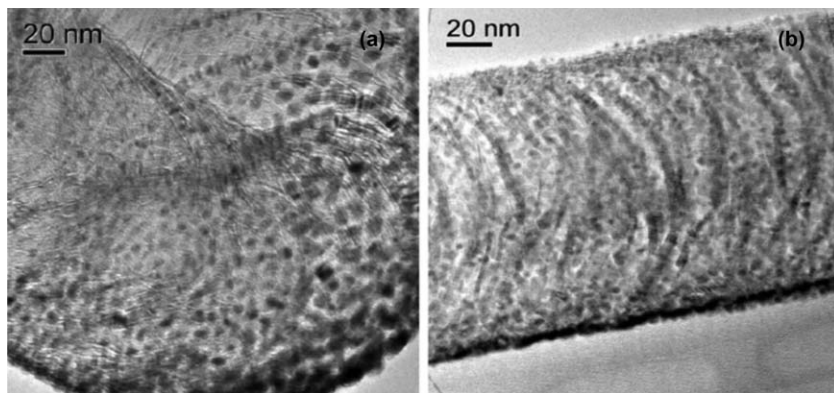
Fig. 15 TEM images of the **(a)** AuNPs/MWCNT (Reproduced from ref. 93 with permission of Elsevier) and **(b)** PtNPs/MWCNT(Reproduced from ref. 95 with kind permission from Springer Science and Business Media).

higher analytical sensitivity than the non-modified equivalent electrode (4.5 fold).[94]

Sputtered PtNPs on vertically aligned MWCNT demonstrated an interesting electroanalytical performance in the determination of L-cysteine.[95] Ye *et al.*[95] proposed the formation of PtNPs on VACNT with similar diameter to that obtained for AuNPs, *i.e.*, 5 nm, as showed in the TEM image in Fig. 15(b). High catalytic performance was diagnostic for the PtNPs/VACNT toward L-cysteine oxidation and, thus, this architecture was successfully employed in the amperometric determination of L-cysteine.

More recently, Xiang *et al.*[96] designed microelectrodes based in platinized VACNT-sheathed carbon fibers (Pt/VACNT-CF) for *in vivo* amperometric monitoring of oxygen. Oxygen electrochemical monitoring was performed due to the excellent electrocatalytic activity of Pt toward oxygen reduction. The Pt/VACNT-CF electrodes were produced following a two-step process. First, the VACNT were synthesized on the CF by pyrolysis of iron phthalocyanine (FePc). Second, the platinum nanoparticles were electrodeposited onto the VACNT-CF. SEM images of the VACNT-CF, Pt/CF and Pt/VACNT-CF are shown in Fig. 16 (a–c). From the cross-sectional SEM image of VACNT-CF (Fig. 16(a)) it is possible to observe that very well aligned and dense packets of CNTs were synthesized on the CF surface. Comparing the morphological profile of Pt nanoparticles electrodeposited on CFs (Fig. 16(b)) and VACNT-CF (Fig. 16(c)), it is notable that more homogeneously and evenly distributed Pt nanoparticles were produced on VACNT-CF than on the CF, probably because of the different electronic and porous properties of these carbon substrates.

The Pt/VACNT-CF electrode exhibited an adsorption and desorption wave for hydrogen typically observed on a clean Pt electrode (Fig. 16(d)). Testing the electrochemical performance of the different electrodic materials toward O_2 reduction, the Pt/VACNT-CF electrode provided a four-electron O_2 reduction process at a more positive potential and
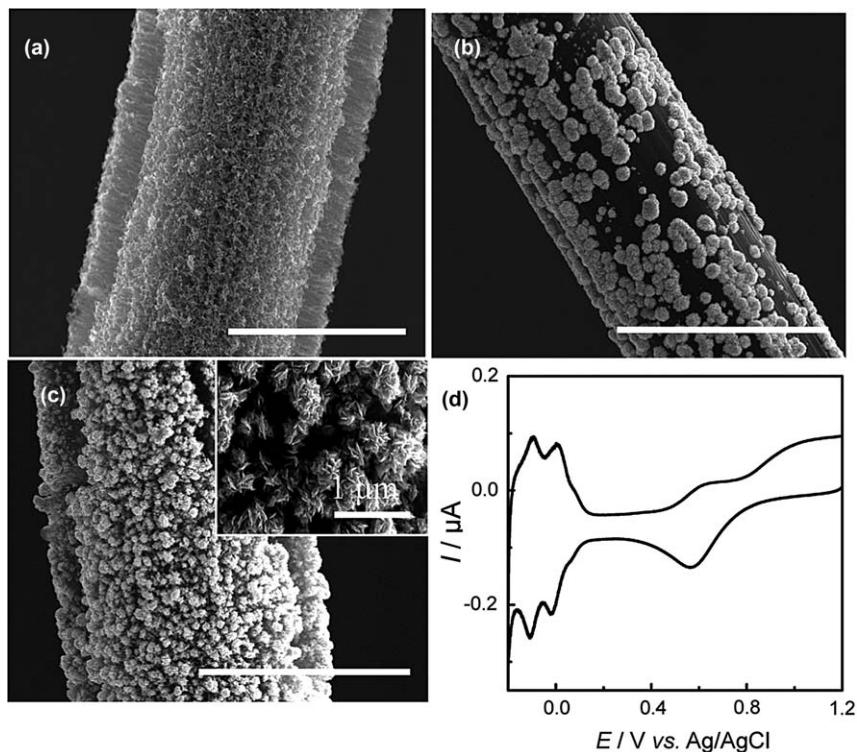
Fig. 16 SEM images of the **(a)** VACNT-CF, **(b)** Pt/CF, and **(c)** Pt/VACNT-CF. [Scale bar in panels (a), (b), and (c) are 10 µm]. Inset in panel (c) shows many densely packed Pt nanoparticles homogeneously distributed on the surface of VACNT. **(d)** Typical cyclic voltammogram (CV) obtained at the Pt/VACNT-CF in 0.5 mol L^{-1} H$_2$SO$_4$ solution. Scan rate = 100 mV s^{-1}. (Reprinted with permission from ref. 96 Copyright (2014) American Chemical Society).

higher current, demonstrating the excellent electrocatalytic properties of the proposed electrode architecture. Furthermore, the sensor showed a good selectivity relative to other electroactive molecules coexisting in the cerebral systems, and a stable O$_2$ amperometric response. Finally, a number of assays were performed to assess *in vivo* O$_2$ monitoring in the brain of rats subjected to various physiological stimuli (ischemia, respiring O$_2$ or N$_2$, and hindfeet pinching). It was verified that the implanted Pt/VACNT-CF microelectrode was sensitive to the O$_2$ variations in the brain during the different physiological stimuli, suggesting its utility for future studies on the neurochemical processes involved in various brain functions.

4.2 Electrochemical biosensors based on VACNT

VACNT electrodes have been successfully employed with different immobilised biological materials, such as enzymes (catalytic biosensors) and antibodies or DNA (affinity biosensors), for the development of electrochemical biosensors. The characteristics of these different electrochemical biosensors are discussed in the next sections.

4.2.1 Enzymatic biosensors. Table 3 summarizes a comprehensive list of enzymatic biosensors based on VACNT electrodes. Yu *et al.*[97] reported that peroxidase had been immobilised covalently onto vertically aligned SWCNT forest array electrodes. The vertically aligned SWCNT forest was first functionalised with carboxyl groups following a two-step process.[98] Initially, commercial SWCNT were subjected to an acid treatment using concentrated HNO_3 and H_2SO_4 acids for 4 h at 70 °C in an ultrasonic bath, in order to insert the carboxyl functional groups on the SWCNT surface. This treatment also shortened the SWCNT length. After that, the previously functionalised SWCNT were vertically aligned onto a pyrolytic graphite electrode previously covered with a Nafion–$Fe(OH)_3$ layer. Horse heart myoglobin (Mb) and horseradish peroxidise (HRP) were immobilised onto the SWCNT surface by using water-soluble carbodiimide 1-(3-(dimethylamino)propyl)-3-ethylcarbodiimide hydrochloride (EDC) to promote amide linkages between the carboxyl-terminated nanotubes and the lysine residue of the proteins. The effectiveness of enzyme immobilisation was monitored by atomic force microscope (AFM) and CV analyses. The comparison of the AFM images obtained for vertically aligned SWCNT before and after the attachment of the enzymes, revealed that, after the Mb or HRP immobilisation, the spiky nanotube forest had been covered by a globular coating reminiscent of polyion aggregates (Fig. 17(a, b)). Using CV measurements conducted in pH 5.5 buffer solution, both the enzymatic electrodes, SWCNT-Mb and SWCNT-HRP, exhibited a redox pair at a potential of −0.21 V (Mb) and −0.25 V (HRP) *vs.* SCE, respectively, which are due to the redox pair Fe(II)/Fe(III) of Mb and HRP. These results indicated the efficient immobilisation of the enzymes on the vertically aligned functionalised SWCNT electrode. Finally, both biosensor architectures were tested for the amperometric determination of H_2O_2. The analytical curves were linear from 1.0 to 10 μmol L^{-1}, with analytical sensitivities of 0.049 μA μmol^{-1} L (SWCNT/HRP) and 0.033 μA μmol^{-1} L (SWNCT/Mb) and limits of detection of 70 nmol L^{-1} and 50 nmol L^{-1} for the SWCNT/Mb and SWNCT/HRP electrodes, respectively. Therefore, a better analytical performance was verified for the HRP-based biosensor, as expected, because HRP presents a better peroxidase activity than Mb. This study demonstrated the viability of using VACNT electrodes for the design of novel enzymatic sensors.

An improvement in the fabrication of the SWCNT forests was obtained by the same research group[99] using a 3-month-old SWCNT dispersion, which provided higher nanotube density and conductivity. The authors fabricated an enzymatic biosensor based on Mb immobilisation or HRP immobilisation onto the end of vertically aligned SWCNT functionalised with carboxyl groups (as previously discussed in ref. 97). A comparison of the amperometric response for hydrogen peroxide of both enzymatic electrodes showed a considerable improvement when using the SWCNT forest prepared with an aged SWCNT dispersion than that obtained using fresh nanotubes to assemble the forests. A 3.5-fold better sensitivity to H_2O_2 was observed, while the limits of detection decreased from 50 nmol L^{-1} to 40 nm L^{-1} for SWNCT/HRP electrode and

Table 3 Enzymatic biosensors architectures designed using VACNT electrodes.

Target analyte	Electrode	Enzyme	Technique	Linearity (mol L^{-1})	LOD (mol L^{-1})	Ref.
Glucose	Nafion/GOD@TiO$_2$/FePc-CNTs	Glucose oxidase	Amperometry	5.0×10^{-5}–4.0×10^{-3}	3.0×10^{-5}	101
Glutamate	VACNT-NEA	Glutamate dehydrogenase	Amperometry	1.0×10^{-8}–2.0×10^{-5} and 2.0×10^{-5}–3.0×10^{-4}	1.0×10^{-8}	103
Glutamate	VACNT	Glutamate dehydrogenase	DPV	1.0×10^{-7}–2.0×10^{-5} and 2.0×10^{-5}–5.0×10^{-4}	6.8×10^{-8}	102
Hydrogen peroxide	SWCNT/HRP	Horseradish peroxidise	Amperometry	1.0×10^{-6}–1.0×10^{-5}	5.0×10^{-9}	97
Hydrogen peroxide	SWCNT/Mb	Myoglobin	Amperometry	1.0×10^{-6}–1.0×10^{-5}	7.0×10^{-8}	97
Hydrogen peroxide	SiO$_2$/Hb-AuNPs/ACNTs	Hemoglobin	Amperometry	4.0×10^{-5}–4.0×10^{-3}	2.2×10^{-5}	100
Hydrogen peroxide	N$_2$/H$_2$-VACNT	Horseradish peroxidise	Amperometry	5.0×10^{-5}–3.0×10^{-2}	—	104
Hydrogen peroxide	CO$_2$-VACNT	Horseradish peroxidise	Amperometry	5.0×10^{-5}–3.0×10^{-2}	—	104
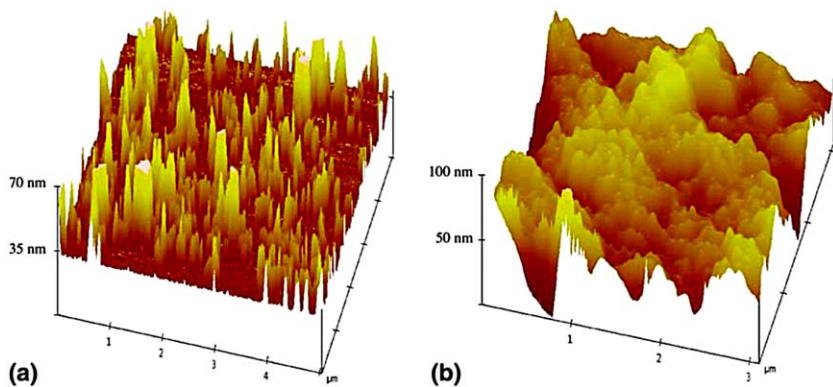
Fig. 17 Tapping mode AFM images of: (a) SWNT forest on smooth silicon and (b) myoglobin-functionalised SWNT forest on silicon (Reproduced from ref. 97 with permission of Elsevier).

increased from 70 nmol L^{-1} to 80 nmol L^{-1} for SWCNT/Mb. The improvement of analytical performance is due the decrease of number of defects in the SWCNT structure and the higher concentration of immobilised enzymes covering the aged SWCNT forest.

An amperometric biosensor for hydrogen peroxide was developed using plasma functionalised VACNT as a platform to immobilise HRP enzyme.[62] VACNT were pretreated using a microwave plasma system (CO_2 and N_2/H_2) to functionalise the nanotubes with oxygenated and aminated groups. From SEM analysis, it was observed that both functionalisation processes improved the stability of VACNT alignment, minimizing the tendency of the CNTs to stick together observed for as-grown VACNT when soaking in aqueous solutions. The improvement of stability was associated with the decreased interaction between the CNT walls, which became weaker after functionalisation of the VACNT surfaces. The VACNT electrodes subjected to the different treatments were tested as platforms for immobilisation of HRP for H_2O_2 biosensing. The HRP was immobilised on the non-modified VACNT surface and on the oxygenated VACNT surface using the classical EDC/NHS reagents. For the nitrogenated VACNT surface, the HRP was immobilised in its oxidized form obtained through a periodation treatment. Those biosensors using plasma-treated VACNT gave better analytical performance, with a sensitivity 3.5-fold higher than that obtained using the biosensor prepared with the as-grown VACNT. This better analytical performance was attributed to the increase of HRP coverage and better direct electron transfer between the enzyme redox centre and the electrode.

Another biosensor to determine H_2O_2 using VACNT, AuNPs, SiO_2 gel and hemoglobin (Hb) (SiO_2/Hb-AuNPs/VACNT electrode), was proposed by Yang et al.[100] The use of AuNPs provided better direct electrochemistry and electrocatalysis of Hb, since the voltammetric response of the Hb's heme Fe(III)/Fe(II) showed a well-defined pair of peaks and higher magnitude of peak currents. Moreover, the use of the SiO_2 gel coating was found to be important to maintain the Hb-AuNP complex immobilised on the VACNT surface. Nevertheless, when the biosensor was fabricated

without SiO$_2$ gel, the hydrophilic properties of Hb and AuNPs promoted their solubilisation in the supporting electrolyte, resulting in an analytical signal disappearance. Exploring the electrocatalytic activity of Hb towards H$_2$O$_2$ reduction, the SiO$_2$/Hb-AuNPs/VACNT electrode was employed for H$_2$O$_2$ determination by amperometry at a potential of -0337 V vs. Ag/AgCl (saturated KCl) reference electrode. The analytical curve was linear in the hydrogen peroxide concentration range from 4.0×10^{-5} to 4.0×10^{-3} mol L^{-1}, with a limit of detection of 2.2×10^{-5} mol L^{-1}. After 28 days, the analytical signal for hydrogen peroxide maintained 91% of its initial response, showing good stability of the biosensor when stored in the 0.1 mol L^{-1} PBS solution at 4 °C.

The immobilisation of glucose oxidase enzyme (GOD) onto a VACNT electrode modified with iron phthalocyanine (FePc) and a nanoporous TiO$_2$ film was investigated by Cui et al.[101] VACNT were synthesized on a Ta substrate by CVD, and the nanotubes were modified by adsorption of FePc on the side and tips of the VACNT. The adsorption and formation of FePc nanoparticles on the VACNT surface could be attributed to π–π interactions. Then, the FePc-VACNT surface was modified with a TiO$_2$ film and, from SEM images, it was verified that the formation of TiO$_2$ nanoparticles at the tips of VACNT had a cauliflower-like shape. The electrochemical redox reactions of the GOD enzyme when immobilised on different electrodes were investigated. For TiO$_2$/FePc-VACNT electrodes with GOD immobilised within a Nafion® (Nafion/GOD@TiO$_2$/FePc-VACNT electrode), a pair of peaks with $E^0 = 0.483$ V was obtained when the potential was cycled in the supporting electrolyte solution (PBS, pH = 7.4). This is an indication of direct electron transfer (DET) of the flavin adenine dinucleotide (FAD) centre of GOD. In contrast, by testing Nafion/GOD@TiO$_2$/FePc-GC or Nafion/GOD@TiO$_2$/VACNT electrodes, the previous GOD redox reaction was not observed, demonstrating the importance of the VACNT and FePc for the DET of GOD. The VACNT improved the conductivity of the nanoporous TiO$_2$ film and the FePc nanoparticles penetrated into the GOD protein shell, facilitating the electron tunneling between the FAD redox centre and the underlying electrode. The Nafion/GOD@TiO$_2$/FePc-VACNT electrode presented an enhanced bioelectrocatalytic activity toward glucose oxidation, and provided a lower response time and higher analytical sensitivity for the amperometric determination of glucose, independently of the presence of oxygen.

Glutamate biosensors based on glutamate dehydrogenase enzyme (GLDH) immobilised on VACNT have been developed by Gholizadeh et al.[102,103] In their first work, a direct immobilisation of GLDH on a VACNT surface was carried out by covalent linkage using EDC and hydrosulfosuccinimide sodium salt (sulfo-NHS) reagents. The GLDH/VACNT electrode and DPV were used to determine glutamate concentration. Under optimized experimental conditions of pH, temperature and concentration of coenzyme, the analytical curve showed two linear ranges for glutamate, i.e. 0.1–20 µmol L^{-1} [sensitivity of 0.976 mA (mmol L^{-1})$^{-1}$ cm^{-2}] and 20–300 µmol L^{-1} [sensitivity of 0.182 mA (mmol L^{-1})$^{-1}$ cm^{-2}] with a limit of detection of 5.7×10^{-8} mol L^{-1}.

In another work, Gholizadeh et al.[103] fabricated a VACNT nanoelectrode array (VACNT-NEA) by photolithography in order to determine glutamate concentration. Better sensitivities [2.2 A (mmol L^{-1})$^{-1}$ cm^{-2} and 0.1A (mmol L^{-1})$^{-1}$ cm^{-2}] and lower LOD of 10 nmol L^{-1} were obtained. Nevertheless, the analytical curves presented the same two linear concentration ranges.

4.2.2 Genosensors. A genosensor or a deoxyribonucleic acid (DNA) biosensor consists of an immobilised DNA probe as the biorecognition element and a transducer, responsible for the conversion of the biological recognition event into a measurable signal.[105] The determinations are based on the specific hybridisation between the immobilised single-stranded DNA (ssDNA) probe with the complementary ssDNA present in the sample solution.[105,106] The combination of nucleic acid layers and electrochemical transducers generated a new class of affinity biosensors of high selectivity and sensitivity toward detection of a number of analytes.[106–108]

A general design of a DNA biosensor and the steps involved in the analyte determination are presented in Fig. 18. Initially, an electrodic surface is modified with a ssDNA probe by a convenient immobilisation method. After that, the DNA biosensor is immersed in a solution containing the target complementary DNA for the occurrence of the specific hybridisation.[109] The hybridisation event is usually detected directly through the change of an electric signal (i.e. current), or indirectly with the help of an enzyme or redox labels. There are three types of DNA
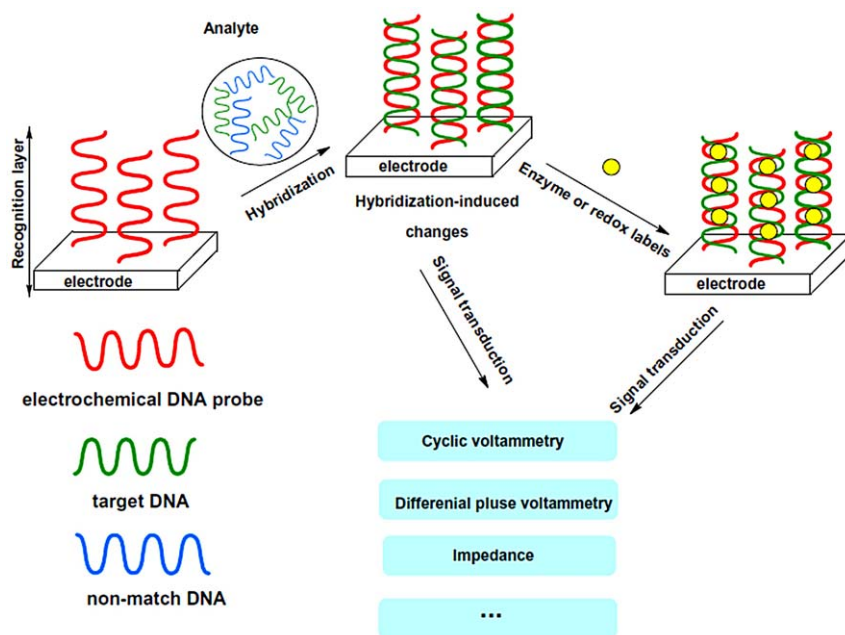
Fig. 18 General design of DNA biosensor (Reproduced from ref. 109 with permission of Elsevier).

biosensors: label-free DNA biosensor, enzyme-labelled DNA biosensor, and label-based DNA biosensor.[110]

The label-free DNA biosensor approach comprises the direct detection of changes of some electrical parameter from the hybridisation event. The first reported use of this kind of genosensor was by Wang *et al.*[111] In this work, the hybridisation event was detected by monitoring the decrease of the guanine peak of an immobilised DNA probe.

For the enzyme-labelled DNA biosensor, an enzyme previously bound to the ssDNA probe triggers the catalysis of a redox reaction and the resulting hybridisation event generates an analytical signal change (*i.e.* a current change for an amperometric transducer).[110]

In label-based (indirect) detection, an electroactive hybridisation indicator binds ssDNA and dsDNA with different affinities, resulting in an unequal concentration in electrode surface, resulting in a change of the electrochemical signal.[110]

The selection of the working electrode is an important parameter for the design of electrochemical genosensors. In this respect, VACNT electrodes have shown promising results, as discussed below.

Li *et al.*[112] synthesized a VACNT array embedded in a SiO_2 matrix by PECVD. The authors suggested that each open-ended VACNT acted as an individual nanoelectrode. This VACNT nanoelectrode was achieved by the production of VACNT arrays with low CNT density, 1×10^8 CNTs/cm^2 with an average tube–tube spacing of 1.5 μm. Using carbodiimide chemistry, the VACNT ends terminated with carboxylic acid groups were functionalised with an oligonucleotide probe with the sequence [Cy3]-5′-CTIIATTTCICAIITCCT-3′[AmC7-Q]. A ssDNA target [Cy5]5′-AGGACCTGCGAAATCCAGGGGGGGGGGGG-3′ which is related to the wild-type allele (Arg1443stop) of the BRCA1 gene were used in this genosensor. Combining the proposed nanoelectrode platform and Ru(bpy)$_3$$^{2+}$ mediated guanine oxidation, a limit of detection of 3.5×10^6 DNA targets (≈ 6 attomoles) was obtained.

Synthetic oligonucleotides (complementary-DNA) were electrochemically detected at nanomolar levels, exploring the interaction between carboxylic group-functionalised VACNT and ssDNA probes.[113] Initially, SWCNT were vertically oriented on a GCE surface using ethylenediamine as a linking agent. Next, the VACNT were functionalised by an acid treatment with HCl and HNO_3, and then the probe ssDNA (pDNA) strands were immobilised on the functionalised VACNT surface, generating ssDNA-wrapped VACNT. The ssDNA-wrapped VACNT were immersed in an acetate buffer solution (pH 5.8) containing complementary ssDNA (cDNA) with gentle agitation for 45 min at 42 °C for hybridisation. The DNA sensing was performed by DPV of the ssDNA-wrapped VACNT. This gave an anodic peak associated with guanine oxidation, after a preconditioning at −0.6V for 60 s. After the hybridisation, the guanine oxidation suffered a significant change as result of formation of the dsDNA structure. The difference in the DPV voltammograms obtained for guanine oxidation of the ssDNA-wrapped VACNT after the hybridisation of cDNA at different concentrations was employed to selectively monitor the cDNA target. Using this approach, cDNA was

determined in the concentration range from 40 to 110 nmol L^{-1}, with a limit of detection of 20 nmol L^{-1}.

Fayazfar *et al.*[114] explored EIS for the development of an impedimetric genosensor based on VACNT and AuNPs for determination of TP53 gene mutation, an important gene in cancer research. The TP53 gene suffers mutations in different types of human cancer, making, therefore, the analysis of the TP53 sequence an interesting strategy for the monitoring of cancer evolution and patient response in therapeutic treatments.

Initially, VACNT were synthesized on a Ta substrate by CVD using ethylenediamine as a precursor and Ni nanoparticles as a catalyst. The VACNT were then purified and functionalised with hydroxyl and carboxyl groups in nitric acid solution using a cyclic voltammetric procedure. Next, AuNPs were electrodeposited onto the VACNT surface by chronoamperometry. The VACNT/AuNPs/Ta electrode was then modified with the thiolated ssDNA probe, by incubation of electrode in a ssDNA buffered solution. This ssDNA/VACNT/AuNPs/Ta electrode was then immersed in solutions containing the DNA target at different concentrations for hybridisation. The EIS measurements were performed for a 5.0 mmol L^{-1} $K_3[Fe(CN)_6]/K_4[Fe(CN)_6]$ in 0.10 mol L^{-1} KCl solution, and the respective values of charge transfer resistance (R_{ct}) correlated with the hybridisation process. From the EIS measurements, it was verified that the charge transfer for the $Fe(CN)_6^{3-}/Fe(CN)_6^{4-}$ redox reaction was hindered when the VACNT/AuNPs/Ta electrode was modified with the ssDNA probe, resulting in an increase of resistance R_{ct}, due the formation of an insulating layer. This effect was more pronounced after the hybridisation of the target DNA sequence, and with increasing target DNA concentration in solution, higher values of R_{ct} were registered. Thus, the analytical signal was defined as the difference between the R_{ct} values obtained for the dsDNA/VACNT/AuNPs/Ta and the ssDNA/VACNT/AuNPs/Ta electrodes (*i.e.* ΔR_{ct}). The Nyquist plots obtained for the ssDNA/VACNT/AuNPs/Ta electrode hybridized with different amounts of complementary target DNA are shown in Fig. 19(a), and the respective analytical curve is presented in Fig. 19(b). The analytical curve was linear in the TP53 concentration range from 1.0×10^{-15} to 1.0×10^{-7} mol L^{-1}, with a limit of detection of 1.0×10^{-17} mol L^{-1}. Moreover, the proposed genosensor demonstrated a good stability, with a decrease of 8.4% of initial response for 14 days of storage time at 4 °C.

4.2.3 Immunosensors. Immunoassays comprise bioanalytical methods in which the determination of the analyte depends on the reaction of an antigen (analyte such as ions, amino acids, antibiotics, vitamins, peptides, drugs, pharmaceutical products, metabolites and so on) and an antibody, with the help of a label, resulting in the production of detectable species. Another possibility is that an immunoassay may use an antigen to determine an antibody which recognizes the antigen (in which case the antibody is the analyte). The specific and selective reaction between a particular antibody and an antigen is the principle behind immunosensing, and electrochemical-type immunosensors
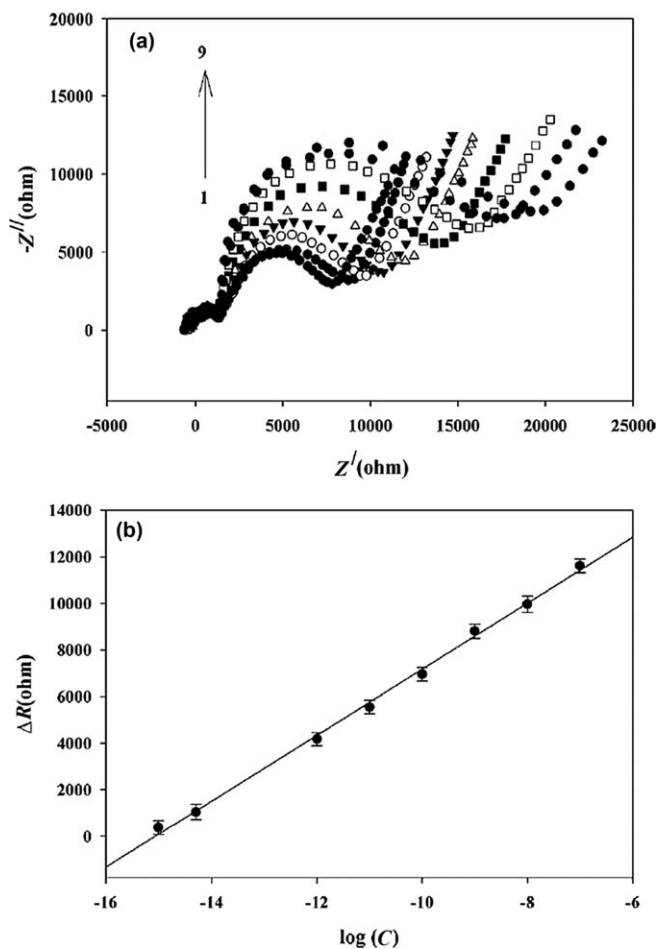
Fig. 19 (a) Nyquist plots for ssDNA/A-MWCNT/AuNPs/Ta electrodes hybridised with the following amounts of complementary DNA: (1) 0, (2) 1.0×10^{-15}, (3) 5.0×10^{-15}, (4) 1.0×10^{-12}, (5) 1.0×10^{-11}, (6) 1.0×10^{-10}, (7) 1.0×10^{-9}, (8) 1.0×10^{-8}, and (9) 1.0×10^{-7} mol L^{-1}. $-Z''$ and Z' are the imaginary and real part respectively of impedance Z. **(b)** Plot of ΔR_{ct} vs. the concentration of target DNA. Conditions: treated time 90 min, hybridisation temperature 42 °C in 5.0 mmol L^{-1} $K_4Fe(CN)_6/K_3Fe(CN)_6$ and 0.1 mol L^{-1} KCl solution (Reproduced from ref. 114 with permission of Elsevier).

depend upon a transducer, such as amperometric, conductometric, impedimetric or potentiometric, to generate a signal.

Herein, we will discuss amperometric immunosensors based on VACNT electrodes. Before we present these immunosensors, it is important to discuss the many types of immunoassay.

Immunoassays vary by the different labels they use. The most common labels include chromophores, fluorophores, radioisotopes and enzymes. Of those labels, enzyme immunoassay or enzyme-linked immunosorbent assay (ELISA) is the most popular technique. ELISA has as an advantage the amplification of the analytical signal and/or increase of the sensitivity of the immunoassay. There are four types of ELISA: direct ELISA, indirect ELISA, sandwich ELISA and competitive ELISA.

The direct ELISA method is considered the simplest type of immuno-assay (Fig. 20). The antigen is adsorbed onto the electrode surface, then an excess of another protein (normally bovine serum albumin, BSA) is added to block all the other binding sites on the surface. An enzyme linked to an antibody in a separate reaction is added, which then produces the enzyme–antibody complex. After that, any excess enzyme antibody complex is washed off. The enzyme substrate is then added and produces an analytical signal directly proportional to the antigen concentration in the sample.

The indirect ELISA utilizes two-step ELISA involving two binding process, such as a primary antibody and a labelled secondary antibody (Fig. 21). A specific antigen in a sample is adsorbed onto the surface. After that, any excess antigen is removed by washing and the surface area not coated with the antigen is blocked with BSA. A primary antibody specific to that antigen is then added, and an antibody–antigen complex is formed. After washing, an enzyme linked to a secondary antibody (antibody enzyme conjugate) is added and, the excess washed off. Finally, the substrate is added, producing a detectable analytical signal directly
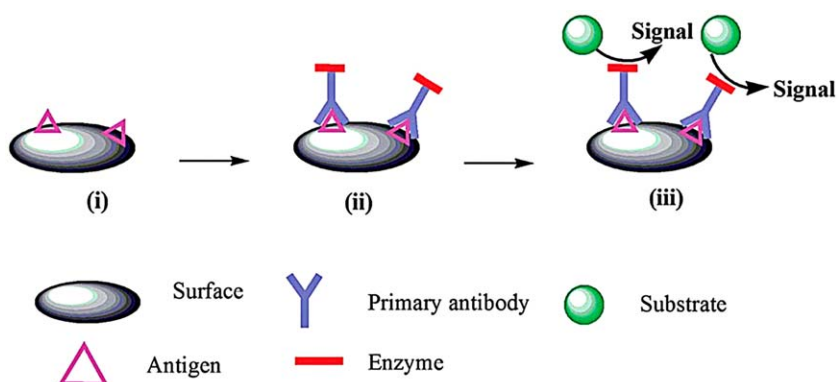
Fig. 20 Scheme of a direct ELISA immunoassay (Reproduced from ref. 115 with permission from The Royal Society of Chemistry).
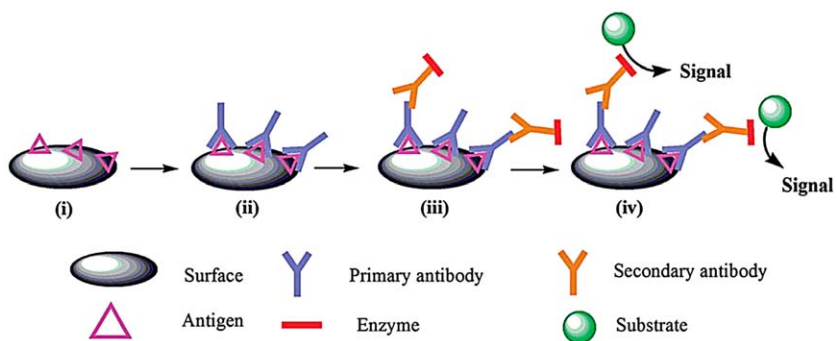
Fig. 21 Scheme of an indirect ELISA immunoassay (Reproduced from ref. 115 with permission from The Royal Society of Chemistry).
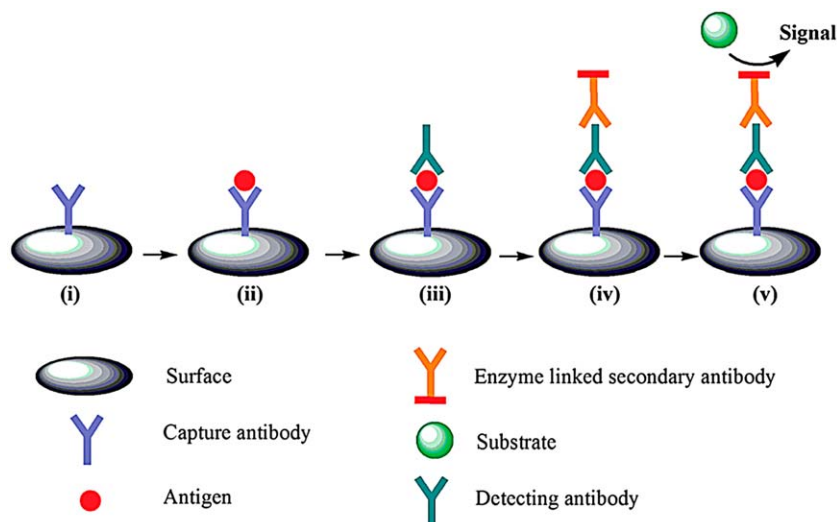
Fig. 22 Scheme of a sandwich ELISA immunoassay (Reproduced from ref. 115 with permission from The Royal Society of Chemistry).

proportional to the antigen concentration in the sample. The advantages of indirect ELISA[115] are its high sensitivity and flexibility, because different primary detection antibodies can be used with a simple labelled secondary antibody. Moreover, since fewer labelled antibody are required; this type of immunoassay is cheaper and faster than direct ELISA.

Sandwich ELISA is the most popular of the ELISA immunoassays. Here, the measurable antigen is sandwiched between two antibodies (a capture antibody and a detection antibody), which bind to different sites on the antigen or ligand (Fig. 22).

A known amount of the capture antibody, which is highly specific for the antigen, is bound to a solid surface, while the non-specific binding sites are blocked by BSA. The antigen is then added and binds the capture antibody; as before any excess is washed off. The second antibody (referred to as the detection antibody) is then added and binds the antigen at a different epitope than the capture antibody (the antigen is sandwiched between two antibodies). Excess capture antibody is washed off and the enzyme-linked secondary antibody is added which binds to the non-specific region of the detection antibody. The excess enzyme-linked secondary antibody is washed off and the substrate is added. The substrate which is converted by the used enzyme generates an analytical signal. When the concentration of antigen in the sample increases, the concentration of detection antibody increases, leading to an increase of the analytical signal. The analytical curve of a sandwich immunoassay has a positive slope.

As in a sandwich ELISA immunoassay a single antigen binds two antibodies, the antigen must have at least two epitopes. The capture and detection antibodies may be ether monoclonal (those that recognize a simple epitope) or polyclonal (those that recognize more than one epitope).
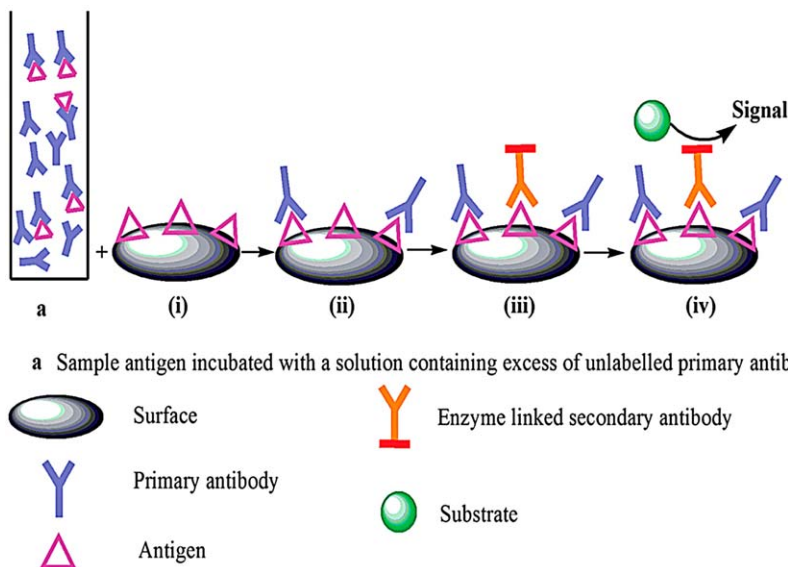
Fig. 23 Scheme of a competitive ELISA immunoassay (Reproduced from ref. 115 with permission from The Royal Society of Chemistry).

The advantage of sandwich ELISA is its high specificity, since a single antigen is captured and detected by two antibodies. This type of immunoassay is more adequate for complex samples, since the antigen does not require any purification before the assay.

In the competitive ELISA immunoassay (Fig. 23), a competitive binding process occurs between the original antigen (sample antigen) and an add-in antigen. In this type of ELISA, the sample antigen is incubated with a solution containing unlabelled primary antibody. These antibody–antigen complexes are then added to a surface pre-coated with the same add-in antigen. Unbound antibody is removed by washing the surface. The secondary antibody that is specific to the primary antibody and conjugated with an enzyme is added. Finally, the substrate is added which is transformed by the enzyme into a detectable analytical signal, which is inversely proportional to the sample antigen concentration.

For this type of ELISA, the higher the sample antigen concentration, the weaker the analytical signal. Competitive ELISA is highly specific as well as sensitive, since two antibodies are used and the sample antigen is selectively captured and detected. This immunoassay also is suitable for crude or impure sample solutions since purification of the antigen is not required.

Exploring the same experimental strategies used before,[97] Rusling and co-workers[99,116–119] developed several immunosensors based on vertically aligned SWCNT electrodes.

O'Connor et al.[116] presented a prototype amperometric immunosensor for determination of horseradish peroxidase labelled biotin (HRP-biotin) and unlabelled biotin by a competitive approach. Initially, vertically aligned functionalised SWCNT were prepared onto a pyrolytic graphite electrode previously covered with a Nafion–Fe(OH)$_3$ layer, as described

elsewere.[59] Then, the anti-biotin antibody (goat polyclonal, B-3640) was added onto the SWCNT forest and allowed to incubate for 3 h. After this incubation period, the surface was washed with PBS solution containing Tween 20 and, finally, with pure PBS solution for removal of the excess antibody. The modified surface was blocked with a 2% bovine serum albumin (BSA) solution prepared in PBS. For the biotin determination by competition, a PBS solution containing both biotin and HRP-biotin was incubated on the BSA-blocked/antibody/SWCNT surface for 1 h. Rotating disc amperometry was performed at -0.3 V $vs.$ SCE at 2000 rpm. The analytical signal was based on the oxidation of HRP by hydrogen peroxide and the catalytic reduction back to its original form by hydroquinone. Using 150 μmol L^{-1} H_2O_2, 300 μmol L^{-1} hydroquinone and 0.5 mg mL^{-1} antibody incubation solution, the analytical curve for HRP-biotin was linear from 1.0 to 25 pmol mL^{-1}, with a limit of detection of 2.5 pmol mL^{-1}. Then, using the optimum concentrations of HRP-biotin (25 pmol mL^{-1}), H_2O_2 (400 μmol L^{-1}) and hydroquinone (1.0 mmol L^{-1}) the competition assays for biotin determination were performed. In this case, the mediated amperometric response of HRP-biotin decreased with increasing free biotin concentration in solution. The analytical curve was linear in the biotin concentration range from 4 nmol mL^{-1} to 120 nmol mL^{-1}, with a limit of detection of 16 nmol mL^{-1} (sic). The lifetime of this immunosensor was one week when stored at 4 °C in a humid aerobic chamber (the analytical signal decrease of only 4% in this period).

Using an improved SWCNT forest electrode containing the aged SWCNT dispersion discussed in 4.2.1, Yu et $al.$[99] fabricated an immunosensor to determine human serum albumin (HSA) in serum. For this, a sandwich electrochemical immunoassay for HSA was employed, as shown in Fig. 24. Initially, $anti$-HSA antibody (Ab_1) was immobilised onto aged SWCNT forests using EDC and NHSS reagents. After that, Ab_1/SWCNT was exposed to HSA standard solution (or a sample containing the analyte HSA) for an incubation time of 60 min. After washing with 0.05% Tween-20 in PBS buffer solution for 20 min and, blocking the remaining sites with 2.0% m/v casein solution, the HSA/Ab_1/SWCNT electrode was incubated with a HRP-labelled $anti$-HAS antibody (Ab_2)
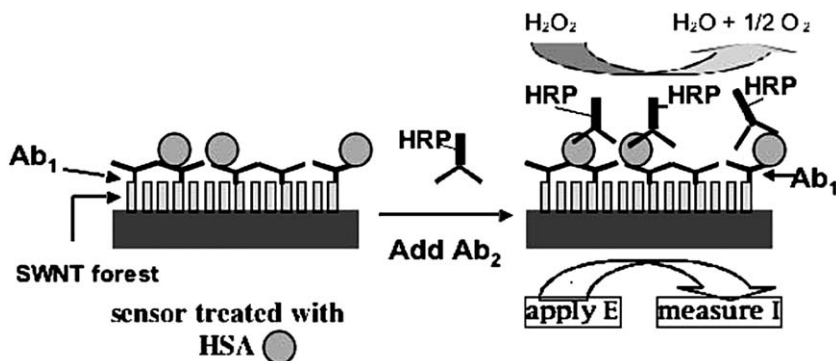
Fig. 24 Schematic diagram of HSA sandwich assay procedure (Reproduced from ref. 99 with permission from The Royal Society of Chemistry).

solution. Using a similar detection protocol[75] as above described, *i.e.*, a rotating disc at a potential of -0.2 V *vs.* SCE and 2000 rpm, 0.4 mmol L^{-1} H$_2$O$_2$ and 0.4 mmol L^{-1} hydroquinone (mediator) the immunosensor presented an analytical curve linear in HSA concentration in the range from 1.5 to 20.0 pmol mL^{-1}, a limit of detection of 1.0 pmol mL^{-1} and a sensitivity of 46 nA pmol^{-1} mL. This shows that these electrodes can be used to monitor HSA in urine samples, which could be very important in the diagnosis of kidney function abnormalities and microalbuminuria in cancer patients.

In an another work, Munge *et al.*[117] compared the applicability of gold nanoparticles (AuNPs) and SWCNT forests as platforms for the preparation of sandwich immunosensors containing immobilised primary anti-human Interleukin-6 (IL-6) antibody (Ab$_1$) and biotinylated secondary antibody (Ab$_2$) bound to streptavidin-HRP, which provided 14–16 HRP labels on each Ab$_2$ (Ab$_2$-biotin-streptavidin-HRP$_{14-16}$), for the determination of the human cancer biomarker Interleukin-6 (IL-6) in serum. The detection was based on an amperometric sandwich immunoassay using a rotating disc at a potential of -0.3 V *vs.* SCE and 3000 rpm. The immunosensor was fabricated with gold nanoparticles and gave a limit of detection of 10 pg mL^{-1} IL6 (500 amol mL^{-1}) in 10 µL calf serum. A LOD of 30 pg mL^{-1} was obtained using a SWCNT immunosensor for the same assay protocol. The analytical curves were linear in the IL-6 concentration range from 20 to 4000 pg mL^{-1} and 40 to 150 pg mL^{-1} for AuNP- and SWCNT-forest-based immunosensors, respectively. Nevertheless, the SWCNT-forest-based immunosensor gave a 2-fold better sensitivity than the AuNP-based immunosensor. The better detectability of the AuNP-based immunosensor is attributed to a larger concentration of captured antibodies.

A very highly sensitive sandwich immunosensor for a cancer biomarker prostate-specific antigen (PSA) in human serum and prostate tissue samples was proposed by Yu *et al.*[118] In the fabrication of this immunosensor, the authors employed a SWCNT forest platform combined with a multilabel antibody–nanotube bioconjugate. This strategy significantly improved the sensitivity of the analytical method ($\sim$ 800 times) and the limit of detection of 40 pg mL^{-1} in 10 mL of calf serum was lower than any commercial PSA assay. A similar strategy using a four-electrode array for simultaneous determination of four different cancer biomarkers (PSA, prostate specific membrane antigen (PSMA), platelet factor-4 (PF-4) and IL-6) was also proposed.[120] An ultrasensitive amperometric immunosensor for oral cancer biomarker IL-6 using the previous strategies of multilabel amplification, based on bioconjugates Ab$_2$-biotin-streptavidin-HRP$_{14-16}$[117] and multi-label antibody–nanotube,[118,120] was developed by Malhotra *et al.*[119] A sandwich imunossensor based on SWCNT forests and the 14–16 system was applied for determination of elevated concentrations of IL-6, specifically in the concentration range obtained by Munge *et al.*[117] Moreover, for IL-6 determination at very low concentration levels, as necessary in the HNSCC cell samples, the multi-label antibody–nanotube bioconjugate system developed for PSA determination[77] was adopted. The analytical curve using this multilabel

amplification strategy was linear in the IL-6 concentration range from 0.5 to 30 pg mL^{-1}, with a LOD of 0.5 pg mL^{-1}. This LOD was 16-fold lower than of conventional ELISA immunoassays.

A new sandwich immunosensor architecture to increase the concentration of enzyme labels uses polystyrene beads for the sensitive determination of matrix metalloproteinase-3 (MMP-3) was proposed by Munge et al.[121] In a typical procedure, anti-MMP-3 antibody (Ab$_1$) was firstly immobilised onto SWCNT forests using EDC and NHSS reagents. After that, Ab$_1$/SWCNT was incubated at 37 °C for 75 min with serum containing MMP-3, followed by washing steps with 0.1% Tween-20 in PBS buffer solution and then with only PBS buffer solution for 1.5 min. Finally, the MMP-3/Ab$_1$/SWCNT electrode was incubated with biotinylated anti-MMP-3 antibody (Ab$_2$) and then with streptavidin modified HRP or Ab$_2$–HRP polystyrene bead bioconjugate. The Ab$_2$–HRP polystyrene bead bioconjugate was based on 500 nm polystyrene beads coated with streptavidin, multiple HRP labels and secondary antibodies (Ab$_2$), providing a high loading of enzyme labels. Due the higher concentration of labels created by the binding event, the immunosensor using the Ab$_2$–HRP polystyrene bead bioconjugate provided an improved analytical performance toward MMP-3 detection. The analytical sensitivity was 65-fold higher than that obtained using the immunosensor based on Ab$_2$–biotin–streptavidin–HRP$_{14-16}$ bioconjugate and the LOD decreased from 0.4 ng mL^{-1} to 4 pg mL^{-1} in 10 μL of calf serum. More recently, Rusling and co-workers[122] developed an ingenious, inexpensive, automated, multiplexed protein immunoarray as a point-of-care diagnostic.

Liu and collaborators designed new electrochemical immunosensors based on chemical assembly of vertically aligned SWCNT on carbon substrates for direct detection of the pesticide endosulfan[123] and the insecticide paraoxon[124] in spiked environmental water samples. In both electrochemical immunosensors, the applied SWCNT forest was fixed onto a GC electrode exploring the formation of amide bonds between the carboxylic functional groups at the SWCNT ends and the amine groups on the GC surface, which was previously modified with mixed layers of 4-aminophenyl and phenyl. This architecture was named as GC-Ph-NH$_2$/SWCNT.

The GC-Ph-NH$_2$/SWCNT surface was modified with 2-[2-[2-(4-aminophenoxy)ethoxy]ethoxy]ethanol (PEG) to avoid the nonspecific protein adsorption and with ferrocenedimethylamine (FDMA) generating, thus, the GC-Ph-NH$_2$/SWCNT/PEG/FMDA electrode. This surface was subjected to an amide coupling reaction with a 1.0 mg mL^{-1} endosulfan hapten in 0.1 mol L^{-1} PBS for 2 h at 4 °C, in order to link the endosulfan hapten to the ferrocene group. Next, the GC-Ph-NH$_2$/SWCNT/PEG/FMDA surface modified with the endosulfan hapten was immersed in a PBS solution containing the endosulfan monoclonal antibody IgG at 4 °C for 30 min. The electrode containing the antiendosulfan IgG (GC-Ph-NH$_2$/SWCNT/PEG/FMDA/endosulfan hapten/ antiendosulfan IgG) thus obtained was exposed to sample solutions containing the analyte endosulfan, and the analytical signal was the peak current obtained from the attached ferrocene group, which suffers modulation during the binding events between antiendosulfan IgG and the analyte endosulfan. The modulation
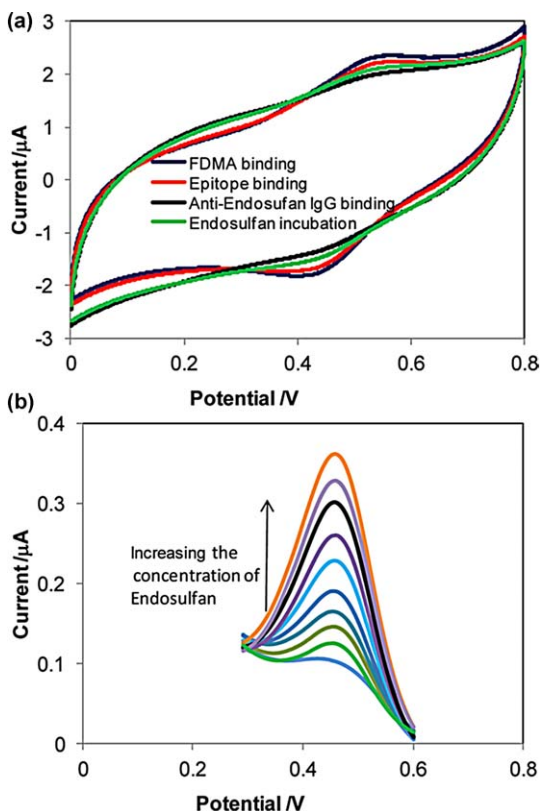
Fig. 25 (a) CVs. of GC-Ph-NH$_2$/SWNT/PEG-modified GC surfaces after the stepwise binding of FDMA, epitope (endosulfan hapten), antiendosulfan IgG, and endosulfan in 0.05 M phosphate buffer (0.05 M KCl, pH 7.0) at a scan rate of 100 mV s^{-1}. (b) SWV curves for GC-Ph-NH$_2$/SWNT/PEG/FDMA/endosulfan hapten/antiendosulfan IgG-modified GC surfaces after incubation in endosulfan solutions with concentrations of 0, 0.02, 0.05, 0.1, 0.2, 0.4, 0.8, 1, 2, and 4 ppb, respectively (Reprinted with permission from ref. 123 Copyright (2012) American Chemical Society).

effect on the ferrocene voltammetric response can be evaluated from the cyclic voltammograms, as shown in Fig. 25(a). The ferrocene group presented practically the same voltammetric response after the modification with the endosulfan hapten. However, peak currents decreased significantly after the incubation of the electrode with the antiendosulfan IgG. After the exposition of the GC-Ph-NH$_2$/SWCNT/PEG/FMDA/endosulfan hapten/antiendosulfan IgG electrode in the sample solution containing endosulfan analyte, the ferrocene peak currents increased again, as result of the affinity between the antiendosulfan IgG and endosulfan, promoting the antiendosulfan IgG dissociation from the endosulfan hapten. The increment of the anodic peak current is directly proportional to the endosulfan concentration in the sample solution (Fig. 25(b)). The obtained analytical curve was linear in the endosulfan concentration range from 0.01 to 20 ppb, with a limit of detection of 0.01 ppb.

Using the same strategy employed for endosulfan determination, Liu et al.[124] developed an amperometric immunosensor for direct detection of insecticide paraoxon. In this work, the analytical curve was linear in

the paraoxon concentration range from 2.0 to 2500 ppm, with a limit of detection of 2 ppb.

5 Conclusions and future perspectives

VACNT growth and surface modifications are the base for the several strategies for the many sensitive electrochemical sensors shown in this chapter. The literature review reveals broad possibilities involving growth methods and surface modification by inclusion of different adsorbents, nanoparticles, enzymes, DNA and so on. Carbon nanotubes have already been shown as a good sensor platform because of their high conductivity, high heterogeneous electron transfer, functionalization capabilities, growth of nanoparticles, and affinity to bio-environments. VACNT electrochemical sensors present even further possibilities. Our own results show that specific growth routes and treatments present different materials with different properties. This means that growth and surface functionalization control are key to developing such sensors.

The analytical performance of electrochemical (bio)sensors based on VACNT present significant improvement over standard flat electrodes. In general, aligned CNTs presented better charge transport and charge transfer than randomly organised CNTs, providing better performance. Moreover, recent results demonstrated that exfoliation of VACNT tips with oxygen plasma provides even higher electroactive surface area and heterogeneous electron transfer rate constant. These VACNT-GO electrodes demonstrate an excellent electrochemical behaviour. The VACNT-GO is also likely to perform suitably in grafting other adsorbents and nanoparticles. VACNT electrodes will continue to find wide application to determine many inorganic and organic compounds of biological, environmental, food and pharmaceutical interest.

References

1   S. Iijima, *Nature*, 1991, **354**, 56.
2   S. Iijima and T. Ichihashi, *Nature*, 1993, **363**, 603.
3   A. G. d. Souza Filho and S. B. Fagan, *Quim. Nova*, 2007, **30**, 1695.
4   J. J. Gooding, *Electrochim. Acta*, 2005, **50**, 3049.
5   A. J. G. Zarbin and M. M. Oliveira, *Quim. Nova*, 2013, **36**, 1533.
6   R. H. Baughman, A. A. Zakhidov and W. A. de Heer, *Science*, 2002, **297**, 787.
7   D. Vairavapandian, P. Vichchulada and M. D. Lay, *Anal. Chim. Acta*, 2008, **626**, 119.
8   N. G. Sahoo, S. Rana, J. W. Cho, L. Li and S. H. Chan, *Prog. Polym. Sci.*, 2010, **35**, 837.
9   P.-C. Ma, N. A. Siddiqui, G. Marom and J.-K. Kim, *Composites, Part A*, 2010, **41**, 1345.
10 X. Ren, C. Chen, M. Nagatsu and X. Wang, *Chem. Eng. J.*, 2011, **170**, 395.
11 J. Wang, *Electroanalysis*, 2005, **17**, 7.
12 J. M. Nugent, K. S. V. Santhanam, A. Rubio and P. M. Ajayan, *Nano Lett.*, 2001, **1**, 87.
13 L.-q. Luo, X.-l. Zou, Y.-p. Ding and Q.-s. Wu, *Sens. Actuators, B*, 2008, **135**, 61.
14 S. Y. Kim, J. Hong, R. Kavian, S. W. Lee, M. N. Hyder, Y. Shao-Horn and P. T. Hammond, *Energy Environ. Sci.*, 2013, **6**, 888.

15   W. Chartarrayawadee, S. Moulton, C. Too, B. Kim, R. Yepuri, T. Romeo and G. Wallace, *J. Appl. Electrochem.*, 2013, **43**, 865.

16   F.-F. He, S.-Y. Xu, M. Nie, G.-P. Jin, F.-M. Ren, H.-Y. Zheng and L. Li, *Ionics*, 2014, **20**, 97.

17   F. F. Hudari, E. H. Duarte, A. C. Pereira, L. H. Dall'Antonia, L. T. Kubota and C. R. T. Tarley, *J. Electroanal. Chem.*, 2013, **696**, 52.

18   C. E. Banks, R. R. Moore, T. J. Davies and R. G. Compton, *Chem. Commun.*, 2004, 1804.

19   R. R. Moore, C. E. Banks and R. G. Compton, *Anal. Chem.*, 2004, **76**, 2677.

20   I. Streeter, G. G. Wildgoose, L. Shao and R. G. Compton, *Sens. Actuators, B*, 2008, **133**, 462.

21   C. E. Banks, A. Crossley, C. Salter, S. J. Wilkins and R. G. Compton, *Angew. Chem., Int. Ed.*, 2006, **45**, 2533.

22   M. Pumera, *Langmuir*, 2007, **23**, 6453.

23   C. Batchelor-McAuley, G. G. Wildgoose, R. G. Compton, L. Shao and M. L. H. Green, *Sens. Actuators, B*, 2008, **132**, 356.

24   E. J. E. Stuart and M. Pumera, *J. Phys. Chem. C*, 2010, **114**, 21296.

25   C. P. Jones, K. Jurkschat, A. Crossley, R. G. Compton, B. L. Riehl and C. E. Banks, *Langmuir*, 2007, **23**, 9501.

26   K. Krischer and E. R. Savinova, in *Handbook of Heterogeneous Catalysis*, ed. G. Ertl, H. Knözinger, F. Schüth and J. Weitkamp, Wiley-VCH, Chichester, 2009, pp. 1873–1905.

27   S. C. S. Lai, A. N. Patel, K. McKelvey and P. R. Unwin, *Angew. Chem., Int. Ed.*, 2012, **51**, 5405.

28   N. Bitri, P. Vincent, L. Buisson, P. Merzeau, J.-P. Salvetat, K. Huang, A. Chovin, C. Demaille, S. Marsaudon and J.-P. Aimé, *Carbon*, 2014, **69**, 113.

29   C. E. Banks and R. G. Compton, *Analyst*, 2006, **131**, 15.

30   C. Gao, Z. Guo, J.-H. Liu and X.-J. Huang, *Nanoscale*, 2012, **4**, 1948.

31   Y. Zhang, Y. Bai and B. Yan, *Drug Discovery Today*, 2010, **15**, 428.

32   S. Daniel, T. P. Rao, K. S. Rao, S. U. Rani, G. R. K. Naidu, H.-Y. Lee and T. Kawai, *Sens. Actuators, B*, 2007, **122**, 672.

33   C. Hu, Y. Zhang, G. Bao, Y. Zhang, M. Liu and Z. L. Wang, *J. Phys. Chem. B*, 2005, **109**, 20072.

34   C. Hsueh and A. Brajter-Toth, *Anal. Chem.*, 1994, **66**, 2458.

35   U. Yogeswaran and S.-M. Chen, *Sens. Actuators, B*, 2008, **130**, 739.

36   B. Wei, L. Zhang and G. Chen, *New J. Chem.*, 2010, **34**, 453.

37   R. J. Chen, Y. Zhang, D. Wang and H. Dai, *J. Am. Chem. Soc.*, 2001, **123**, 3838.

38   M. A. Aziz, S. Park, S. Jon and H. Yang, *Chem. Commun.*, 2007, 2610.

39   W. Feng and P. Ji, *Biotechnol. Adv.*, 2011, **29**, 889.

40   F. Liang and B. Chen, *Curr. Med. Chem.*, 2010, **17**, 10.

41   M. B. Lerner, N. Kybert, R. Mendoza, R. Villechenon, M. A. B. Lopez and A. C. Johnson, *Appl. Phys. Lett.*, 2013, **102**, 183113.

42   A. Chou, T. Bocking, N. K. Singh and J. J. Gooding, *Chem. Commun.*, 2005, 842.

43   A. G. Crevillen, M. Pumera, M. C. Gonzalez and A. Escarpa, *Analyst*, 2009, **134**, 657.

44   R. Marcus, *Annu. Rev. Phys. Chem.*, 1964, **15**, 155.

45   H. Gerischer, ed. H. Eyring, D. Henderson and W. Jost, Academic Press, New York, 1970, vol. 9A, p. 463.

46   A. J. Bard and L. R. Faulkner, *Electrochemical Methods: Fundamentals and Applications*, John Wiley & Sons Inc, New York, 2001.

47   I. Heller, J. Kong, K. A. Williams, C. Dekker and S. G. Lemay, *J. Am. Chem. Soc.*, 2006, **128**, 7353.

48   R. L. McCreery, *Chem. Rev.*, 2008, **108**, 2646.

49 W. Z. Li, S. S. Xie, L. X. Qian, B. H. Chang, B. S. Zou, W. Y. Zhou, R. A. Zhao and G. Wang, *Science*, 1996, **274**, 1701.

50 Z. Ren, Z. Huang, J. Xu, J. Wang, P. Bush, M. Siegal and P. Provencio, *Science*, 1998, **282**, 1105.

51 M. Gao, L. Dai and G. G. Wallace, *Electroanalysis*, 2003, **15**, 1089.

52 J. Okuno, K. Maehashi, K. Matsumoto, K. Kerman, Y. Takamura and E. Tamiya, *Electrochem. Commun.*, 2007, **9**, 13.

53 N. G. Tsierkezos and U. Ritter, *J. Solid State Electrochem.*, 2010, **14**, 1101.

54 K. Gong, S. Chakrabarti and L. Dai, *Angew. Chem., Int. Ed.*, 2008, **47**, 5446.

55 Y. Wang, G. Du, L. Zhu, H. Liu, C.-P. Wong and J. Wang, *Sens. Actuators, B*, 2012, **174**, 570.

56 H. Zanin, P. W. May, R. L. Harniman, T. Risbridger, E. J. Corat and D. J. Fermin, *Carbon*, 2014, **82**, 288.

57 H. Zanin, P. W. May, D. J. Fermin, D. Plana, S. M. C. Vieira, W. I. Milne and E. J. Corat, *ACS Appl. Mater. Interfaces*, 2013, **6**, 990.

58 T. A. Silva, H. Zanin, P. W. May, E. J. Corat and O. Fatibello-Filho, *ACS Appl. Mater. Interfaces*, 2014, **6**, 21086.

59 S. C. Ramos, Doutorado em Engenharia e Tecnologia Espaciais Tese de Doutorado em Engenharia e Tecnologia Espaciais, Instituto Nacional de Pesquisas Espaciais, 2011.

60 H. Zanin, E. Saito, H. J. Ceragioli, V. Baranauskas and E. J. Corat, *Mater. Res. Bull.*, 2014, **49**, 487.

61 S. C. Ramos, G. Vasconcelos, E. F. Antunes, A. O. Lobo, V. J. Trava-Airoldi and E. J. Corat, *Diamond Relat. Mater.*, 2010, **19**, 752.

62 D. K. Owens and R. C. Wendt, *J. Appl. Polym. Sci.*, 1969, **13**, 1741.

63 http://www.unipress.waw.pl/fityk.

64 H. Zanin, P. W. May, M. H. M. O. Hamanaka and E. J. Corat, *ACS Appl. Mater. Interfaces*, 2013, **5**, 12238.

65 M. V. Naseh, A. Khodadadi, Y. Mortazavi, O. A. Sahraei, F. Pourfayaz and S. M. Sedghi, *World Acad. Sci. Eng. Technol.*, 2009, **49**, 177.

66 Y. Tzeng, T. S. Huang, Y. Chen, C. Liu and Y. K. Liu, *New Diamond Front. Carbon Technol.*, 2004, **14**, 193.

67 S. Ramos, G. Vasconcelos, E. Antunes, A. Lobo, V. Trava-Airoldi and E. Corat, *Surf. Coat. Technol.*, 2010, **204**, 3073.

68 A. O. Lobo, H. Zanin, I. A. W. B. Siqueira, N. C. S. Leite, F. R. Marciano and E. J. Corat, *Mater. Sci. Eng., C*, 2013, **33**, 4305.

69 E. Antunes, A. Lobo, E. Corat, V. Trava-Airoldi, A. Martin and C. Veríssimo, *Carbon*, 2006, **44**, 2202.

70 V. Carozo, C. M. Almeida, E. H. Ferreira, L. G. Cancado, C. A. Achete and A. Jorio, *Nano Lett.*, 2011, **11**, 4527.

71 L. Cancado, K. Takai, T. Enoki, M. Endo, Y. Kim, H. Mizusaki, A. Jorio, L. Coelho, R. Magalhaes-Paniago and M. Pimenta, *Appl. Phys. Lett.*, 2006, **88**, 163106.

72 M. S. Dresselhaus, A. Jorio, M. Hofmann, G. Dresselhaus and R. Saito, *Nano Lett.*, 2010, **10**, 751.

73 F. C. Moraes, T. A. Silva, I. Cesarino, M. R. V. Lanza and S. A. S. Machado, *Electroanalysis*, 2013, **25**, 2092.

74 C. Karuwan, A. Wisitsoraat, A. Sappat, K. Jaruwongrungsee, V. Patthanasettakul and A. Tuantranont, *Sens. Lett.*, 2010, **8**, 645.

75 H. Javed, M. M. Khan, A. Ahmad, K. Vaibhav, M. E. Ahmad, A. Khan, M. Ashafaq, F. Islam, M. S. Siddiqui and M. M. Safhi, *Neuroscience*, 2012, **210**, 340.

76 M.-L. Ye, B. Xu and W.-D. Zhang, *Sens. Lett.*, 2013, **11**, 321.

77   A. Corsini, S. Bellosta, R. Baetta, R. Fumagalli, R. Paoletti and F. Bernini, *Pharmacol. Ther.*, 1999, **84**, 413.

78   A. Moscardó, J. Vallés, A. Latorre, I. Madrid and M. T. Santos, *Thromb. Res.*, 2013, **131**, e154.

79   H. Fayazfar, A. Afshar, A. Dolati and M. Ghalkhani, *J. Appl. Electrochem.*, 2014, **44**, 263.

80   T. A. Silva, H. Zanin, F. C. Vicentini, E. J. Corat and O. Fatibello-Filho, *Analyst*, 2014, **139**, 2832.

81   T. A. Silva, H. Zanin, F. C. Vicentini, E. J. Corat and O. Fatibello-Filho, *Sens. Actuators, B*, 2015.

82   E. Saito, E. F. Antunes, H. Zanin, F. R. Marciano, A. O. Lobo, V. J. Trava-Airoldi and E. J. Corat, *J. Electrochem. Soc.*, 2014, **161**, H321.

83   J. Yang, L.-C. Jiang, W.-D. Zhang and S. Gunasekaran, *Talanta*, 2010, **82**, 25.

84   L.-C. Jiang and W.-D. Zhang, *Biosens. Bioelectron.*, 2010, **25**, 1402.

85   J. Yang, W.-D. Zhang and S. Gunasekaran, *Biosens. Bioelectron.*, 2010, **26**, 279.

86   W.-D. Zhang, J. Chen, L.-C. Jiang, Y.-X. Yu and J.-Q. Zhang, *Microchim. Acta*, 2010, **168**, 259.

87   Z. G. Zhu, L. Garcia-Gancedo, C. Chen, X. R. Zhu, H. Q. Xie, A. J. Flewitt and W. I. Milne, *Sens. Actuators, B*, 2013, **178**, 586.

88   W.-S. Kim, G.-J. Lee, J.-H. Ryu, K. Park and H.-K. Park, *RSC Adv.*, 2014, **4**, 48310.

89   C. Li, J. Han and C. H. Ahn, *Biosens. Bioelectron.*, 2007, **22**, 1988.

90   F. Xiao, Y. Li, X. Zan, K. Liao, R. Xu and H. Duan, *Adv. Funct. Mater.*, 2012, **22**, 2487.

91   L.-C. Jiang and W.-D. Zhang, *Electroanalysis*, 2009, **21**, 1811.

92   L.-C. Jiang and W.-D. Zhang, *Electroanalysis*, 2009, **21**, 988.

93   J. Wang and W.-D. Zhang, *J. Electroanal. Chem.*, 2011, **654**, 79.

94   J.-C. Ma and W.-D. Zhang, *Microchim. Acta*, 2011, **175**, 309.

95   M.-L. Ye, B. Xu and W.-D. Zhang, *Microchim. Acta*, 2011, **172**, 439.

96   L. Xiang, P. Yu, M. Zhang, J. Hao, Y. Wang, L. Zhu, L. Dai and L. Mao, *Anal. Chem.*, 2014, **86**, 5017.

97   X. Yu, D. Chattopadhyay, I. Galeska, F. Papadimitrakopoulos and J. F. Rusling, *Electrochem. Commun.*, 2003, **5**, 408.

98   D. Chattopadhyay, I. Galeska and F. Papadimitrakopoulos, *J. Am. Chem. Soc.*, 2001, **123**, 9451.

99   X. Yu, S. N. Kim, F. Papadimitrakopoulos and J. F. Rusling, *Mol. BioSyst.*, 2005, **1**, 70.

100 J. Yang, Y. Xu, P. He and Y. Fang, *Electroanalysis*, 2013, **25**, 2345.

101 H.-F. Cui, K. Zhang, Y.-F. Zhang, Y.-L. Sun, J. Wang, W.-D. Zhang and J. H. T. Luong, *Biosens. Bioelectron.*, 2013, **46**, 113.

102 A. Gholizadeh, S. Shahrokhian, A. Iraji zad, S. Mohajerzadeh, M. Vosoughi, S. Darbari and Z. Sanaee, *Biosens. Bioelectron.*, 2012, **31**, 110.

103 A. Gholizadeh, S. Shahrokhian, A. Iraji Zad, S. Mohajerzadeh, M. Vosoughi, S. Darbari, J. Koohsorkhi and M. Mehran, *Anal. Chem.*, 2012, **84**, 5932.

104 E. Luais, C. Thobie-Gautier, A. Tailleur, M. A. Djouadi, A. Granier, P. Y. Tessier, D. Debarnot, F. Poncin-Epaillard and M. Boujtita, *Electrochim. Acta*, 2010, **55**, 7916.

105 M. I. Pividori, A. Merkoçi and S. Alegret, *Biosens. Bioelectron*, 2000, **15**, 291.

106 A. Erdem, in *Comprensive Analytical Chemistry*, ed. S. Alegret and A. Merkoçi, Elsevier, 2007, vol. 49, ch. 19, p. 403.

107   M. Mascini, I. Palchetti and G. Marrazza, *Fresenius' J. Anal. Chem.*, 2001, **369**, 15.
108   G. Evtugyn, A. Mingaleva, H. Budnikov, E. Stoikova, V. Vinter and S. Eremin, *Anal. Chim. Acta*, 2003, **479**, 125.
109   A. Liu, K. Wang, S. Weng, Y. Lei, L. Lin, W. Chen, X. Lin and Y. Chen, *TrAC, Trends Anal. Chem.*, 2012, **37**, 101.
110   F. R. R. Teles and L. P. Fonseca, *Talanta*, 2008, **77**, 606.
111   J. Wang, M. Jiang, A. Fortes and B. Mukherjee, *Anal. Chim. Acta*, 1999, **402**, 7.
112   J. Li, H. T. Ng, A. Cassell, W. Fan, H. Chen, Q. Ye, J. Koehne, J. Han and M. Meyyappan, *Nano Lett.*, 2003, **3**, 597.
113   X. Zhang, K. Jiao, S. Liu and Y. Hu, *Anal. Chem.*, 2009, **81**, 6006.
114   H. Fayazfar, A. Afshar, M. Dolati and A. Dolati, *Anal. Chim. Acta*, 2014, **836**, 34.
115   K. K. Mistry, K. Layek, A. Mahapatra, C. RoyChaudhuri and H. Saha, *Analyst*, 2014, **139**, 2289.
116   M. O'Connor, S. N. Kim, A. J. Killard, R. J. Forster, M. R. Smyth, F. Papadimitrakopoulos and J. F. Rusling, *Analyst*, 2004, **129**, 1176.
117   B. S. Munge, C. E. Krause, R. Malhotra, V. Patel, J. Silvio Gutkind and J. F. Rusling, *Electrochem. Commun.*, 2009, **11**, 1009.
118   X. Yu, B. Munge, V. Patel, G. Jensen, A. Bhirde, J. D. Gong, S. N. Kim, J. Gillespie, J. S. Gutkind, F. Papadimitrakopoulos and J. F. Rusling, *J. Am. Chem. Soc.*, 2006, **128**, 11199.
119   R. Malhotra, V. Patel, J. P. Vaqué, J. S. Gutkind and J. F. Rusling, *Anal. Chem.*, 2010, **82**, 3118.
120   B. V. Chikkaveeraiah, A. Bhirde, R. Malhotra, V. Patel, J. S. Gutkind and J. F. Rusling, *Anal. Chem.*, 2009, **81**, 9129.
121   B. S. Munge, J. Fisher, L. N. Millord, C. E. Krause, R. S. Dowd and J. F. Rusling, *Analyst*, 2010, **135**, 1345.
122   K. Kadimisetty, S. Malla, N. P. Sardesai, A. A. Joshi, R. C. Faria, N. H. Lee and J. F. Rusling, *Anal. Chem.*, 2015, **87**, 4472.
123   G. Liu, S. Wang, J. Liu and D. Song, *Anal. Chem.*, 2012, **84**, 3921.
124   G. Liu, D. Song and F. Chen, *Talanta*, 2013, **104**, 103.